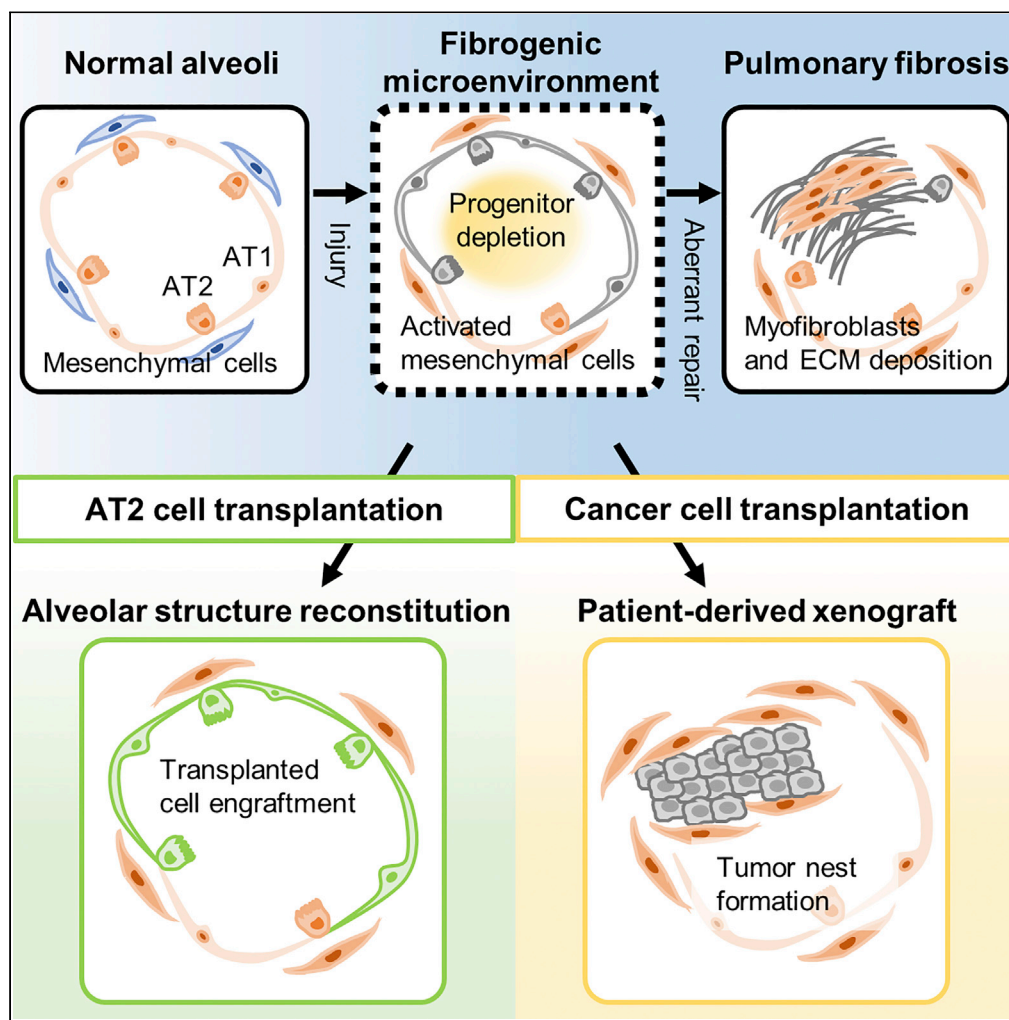# iScience

Article

Lung fibrogenic microenvironment in mouse reconstitutes human alveolar structure and lung tumor

Ryo Miyata, Koichi Hasegawa, Toshi Menju, ..., Toyohiro Hirai, Hiroshi Date, Atsuyasu Sato

atsuyasu@kuhp.kyoto-u.ac.jp

Highlights

Severe bleomycin-induced lung injury causes a significant AT2 cell loss

Mesenchymal cells in the fibrogenic lung supports AT2 cell proliferation

AT2 cell transplantation ameliorates bleomycin-induced pulmonary fibrosis

Novel orthotopic lung cancer models are established for patient-derived xenografts

Article

Lung fibrogenic microenvironment in mouse reconstitutes human alveolar structure and lung tumor

Ryo Miyata,[1,5] Koichi Hasegawa,[2,5] Toshi Menju,[1] Akihiko Yoshizawa,[3] Akira Watanabe,[4] Toyohiro Hirai,[2] Hiroshi Date,[1] and Atsuyasu Sato[2,6,*]

SUMMARY

A mesenchymal cell activation is a hallmark event of pulmonary fibrosis. Alveolar type 2 (AT2) cells are progenitor cells that maintain alveolar homeostasis, and their damage is assumed to be an initiating event for pulmonary fibrosis. However, the interaction between the lung fibrogenic microenvironment and AT2 cell dynamics remains to be elucidated. Here, we report a unique role of the lung fibrogenic microenvironment, where cell type-specific tissue reconstruction is achieved by exogenous cell transplantation. We found that in the lung fibrogenic microenvironment the AT2 cell pool was depleted, whereas mesenchymal cells could promote intact AT2 cell proliferation *in vitro*. Furthermore, exogenously transplanted AT2 cells formed alveolar colonies and ameliorated pulmonary fibrosis. Exogenous tumor cells formed tumor nests with relevant histological and transcriptional properties. Human primary cells were adaptable to this microenvironment, facilitating epithelial cell-targeted therapy in pulmonary fibrosis and the establishment of patient-derived xenografts for precision medicine in lung cancer.

INTRODUCTION

The lung is a vital and complex organ with multiple cell types specifically designed for efficient gas exchange between the outside environment and the blood. The alveoli, the most distal part of the respiratory tract where gas exchange takes place, are covered with two types of epithelial cells: alveolar type 1 (AT1) cells and alveolar type 2 (AT2) cells. These epithelial cells are located in close proximity to other types of cells, such as fibroblasts and endothelial cells, forming an alveolar microenvironment together with an extracellular matrix (ECM) (Fehrenbach, 2001).

Because alveoli are consistently exposed to various stimuli from outside, the mechanism of self-repair is important in the maintenance of lung homeostasis. Previous studies suggest that damage or dysfunction of AT2 cells, which act as progenitor cells in the alveoli (Barkauskas et al., 2013), initiates profibrotic reactions in the lung (Garcia et al., 2016; Nureki et al., 2018; Povedano et al., 2015; Sisson et al., 2010). For example, direct AT2 cell depletion in mice leads to the development of pulmonary fibrosis (Garcia et al., 2016; Sisson et al., 2010), and mice with mutant surfactant protein C expression in AT2 cells spontaneously develop pulmonary fibrosis (Nureki et al., 2018). Furthermore, mice with telomere dysfunction in AT2 cells are reportedly vulnerable to fibrotic injury (Povedano et al., 2015). These findings support the causal relationship between AT2 cell dysfunction and fibrosis development. However, the dynamics of AT2 cells after exposure to fibrotic injury have not been fully elucidated, and the therapeutic measures for pulmonary fibrosis have been mainly focused on the attenuation of fibroblast activation, which results in the slowing of disease progression (Rogliani et al., 2016). Understanding epithelial cell behavior during the development of fibrotic lung remodeling would be helpful for regenerating alveolar epithelial cell integrity and for developing epithelial cell-targeted therapy.

Lung mesenchymal cells are a heterogeneous population and create a unique microenvironment in the lung. Some cells, such as myofibroblasts, produce excessive amounts of ECM components and impair lung function in pulmonary fibrosis (Sgalla et al., 2018), whereas others have been suggested to contribute

[1]Department of Thoracic Surgery, Graduate School of Medicine, Kyoto University, 54 Kawahara-cho, Shogoin, Sakyo-ku, Kyoto 606-8507, Japan

[2]Department of Respiratory Medicine, Graduate School of Medicine, Kyoto University, 54 Kawahara-cho, Shogoin, Sakyo-ku, Kyoto 606-8507, Japan

[3]Department of Diagnostic Pathology, Graduate School of Medicine, Kyoto University, 54 Kawahara-cho, Shogoin, Sakyo-ku, Kyoto 606-8507, Japan

[4]Center for iPS Cell Research & Application, Kyoto University, 53 Kawahara-cho, Shogoin, Sakyo-ku, Kyoto 606-8507, Japan

[5]These authors contributed equally

[6]Lead contact

*Correspondence: atsuyasu@kuhp.kyoto-u.ac.jp

https://doi.org/10.1016/j.isci.2022.104912

to alveolar regeneration by promoting AT2 cell growth and differentiation into AT1 cells (Barkauskas et al., 2013; Chen et al., 2012; Zacharias et al., 2018). Mesenchymal cells are also associated with the tumor microenvironment. Cancer-associated fibroblasts (CAFs) (Mediavilla-Varela et al., 2016), which secrete ECM, chemokines, cytokines, and tumor growth factors, are one of the key components of tumor-supporting cells. They contribute to tumor growth and tumor invasion through matrix remodeling and the secretion of various soluble factors (Sahai et al., 2020). Of interest, in pulmonary fibrosis, alveolar epithelial cell proliferation is also observed histologically (Weng et al., 2014). Furthermore, pulmonary fibrosis is a risk factor for lung cancer development (Karampitsakos et al., 2017). These facts imply that the lung fibrogenic microenvironment not only plays a role in progressive fibrogenesis but also influences local epithelial cell behavior in both reparative and pathological ways.

Here, we hypothesized that the lung fibrogenic microenvironment has a role in alveolar epithelial cell dynamics. Using a bleomycin (BLM)-induced acute lung injury model, we evaluated AT2 cell behavior and the role of the lung fibrogenic microenvironment in alveolar epithelial cell regeneration in an *in vivo* study and *in vitro* 3D organoid culture. We also applied a unique AT2 cell transfer experiment *in vivo* to elucidate the dynamics of intact AT2 cells in the fibrotic lung microenvironment. To further elucidate this microenvironment, a cancer cell transfer experiment *in vivo* was conducted. Our data showed that AT2 cells in the BLM model were severely depleted *in vivo* and were not responsive to the pro-proliferative microenvironment created by activated lung mesenchymal cells, which promoted the proliferation of intact AT2 cells *in vitro*. Intratracheally transplanted intact AT2 cells reconstituted alveolar epithelial structures adjacent to fibrotic areas, which successfully ameliorated pulmonary fibrosis. Similarly, lung cancer cells transferred to fibrotic lungs engrafted and formed multiple cancer foci, which led to the establishment of orthotopic lung cancer models, including patient-derived xenografts (L-PDXs). Taken together, our studies highlight the fibrogenic lung microenvironment, which promotes autonomous tissue reconstruction by AT2 cells and cancer cells. This information would provide a basis for novel therapeutic approaches in pulmonary fibrosis or tools for precision medicine and drug development against lung cancer.

RESULTS

Low-dose BLM facilitates alveolar regeneration without alveolar collapse

BLM-induced lung injury comprises epithelial and endothelial cell damage followed by alveolar collapse and aberrant ECM deposition in the lung (Hay et al., 1991; Moeller et al., 2008; Rock et al., 2011). By its ability to cleave DNA (Suzuki et al., 1969), BLM induces alveolar epithelial cell injury (Hagimoto et al., 1997; Wang et al., 2000). AT2 cells have been considered to be more damage-resistant than AT1 cells (Herzog et al., 2008). Hypothesizing that a reduction in BLM dosage attenuates AT2 cell damage and promotes alveolar regeneration, we created a low-dose BLM model, where the dose of BLM was reduced to one-quarter of that used in a high-dose model. In the low-dose model, alveolar structures were relatively well maintained (Figure 1A), as evidenced by the significantly lower Ashcroft score compared to that in the high-dose model (Figure 1B) 21 days after BLM administration. Of interest, collagen staining showed significant collagen deposition in normal-appearing alveolar walls in the low-dose model. In the high-dose model, collagen deposition was mostly observed in collapsed alveolar regions (Figure 1C). The collagen content of the lungs, as quantified by the hydroxyproline assay, was significantly higher in the low-dose model than in control mice. Notably, it was not significantly different compared to that in the high-dose model (Figure 1D). These results suggest that collagen production and deposition might be processes that are not only involved in fibrotic remodeling but also in the maintenance of alveolar structures during alveolar regeneration.

Non-AT2 cells are recruited to replenish the AT2 cell pool after high-dose BLM injury

Next, we sought to elucidate the alveolar epithelial cell dynamics following BLM administration. Two different doses of BLM were applied to two lineage trace model mice: Sftpc-CreER^{T2}/ROSA$^{mT/mG}$ mice and Scgb1a1-rtTA/(tetO)$_7$CMV-Cre/ROSA$^{mT/mG}$ mice. In Sftpc-CreER^{T2}/ROSA$^{mT/mG}$ mice, 98.0 ± 0.2% (n = 7) of AT2 cells were positive for GFP expression after tamoxifen-induced Cre-mediated recombination (Figure S1), whereas in Scgb1a1-rtTA/(tetO)$_7$CMV-Cre mice, most AT2 cells (97.4 ± 0.3%, n = 4) as well as a subset of club cells displayed GFP expression following the addition of doxycycline to the chow as previously described (Hasegawa et al., 2017), enabling lineage tracing of both AT2 cells and club cells. On day 21 after low-dose BLM administration, immunofluorescence of the lung in both strains showed well-maintained alveolar structures composed of lineage-positive AT1 cells Figure 1E), indicating regeneration of AT1 cells after injury. In contrast, in the high-dose model of Sftpc-CreER^{T2}/ROSA$^{mT/mG}$ mice, in addition to lineage-positive AT1 cells, lineage-negative AT2 cells accumulated mostly around or within fibrotic
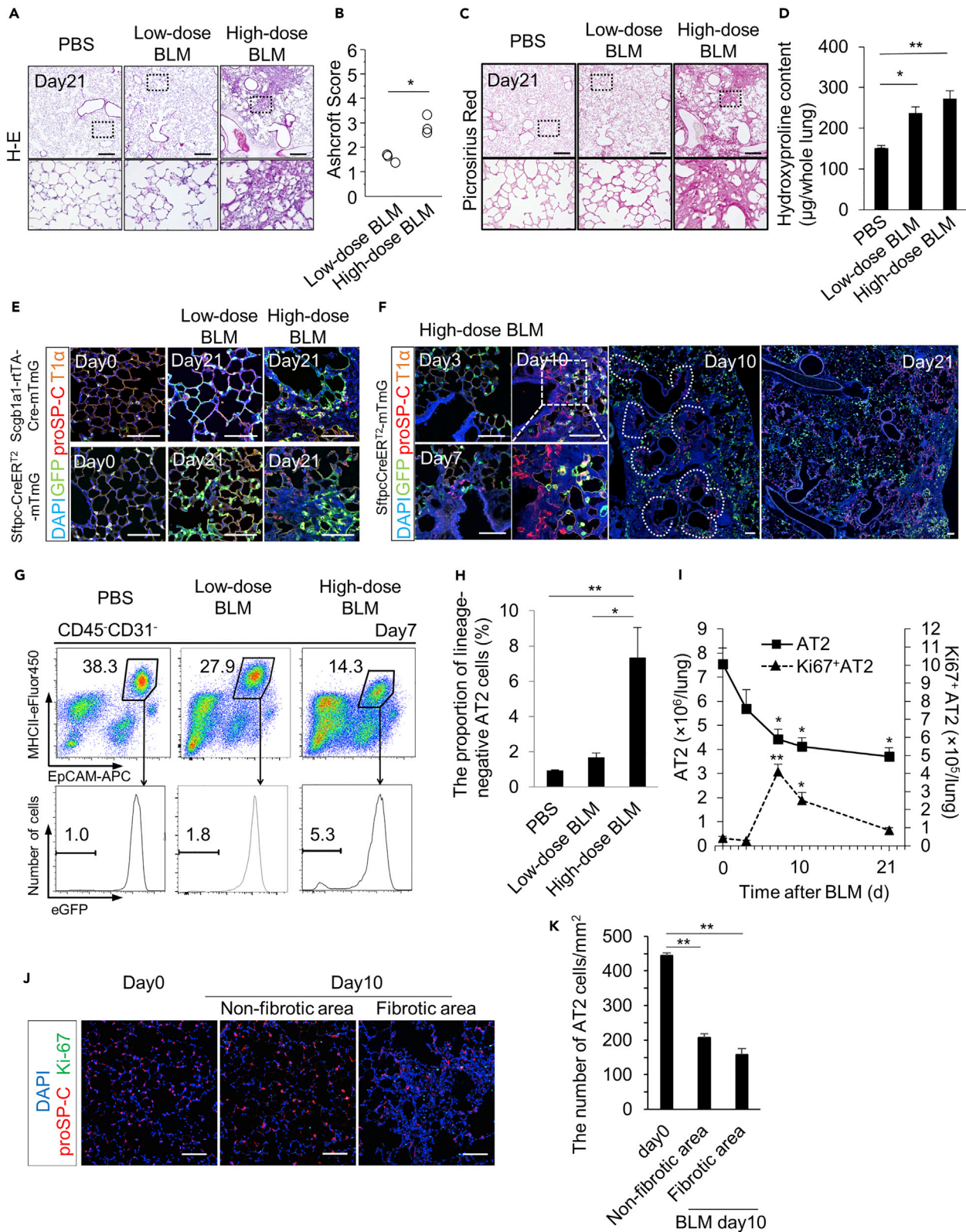
Figure 1. Severe lung injury causes significant AT2 cell loss in the fibrotic lungs

(A) H–E staining of the lung shows that alveolar structures are relatively well maintained in the low-dose BLM model, whereas in the high-dose BLM model massive alveolar collapse occurs on day 21.

(B) The Ashcroft score in the low-dose BLM model was significantly lower than that in the high-dose BLM model on day 21 (n = 3 in each group).

(C) Picrosirius red staining shows collagen deposition in the alveolar walls in the low-dose BLM model and collapsed alveolar regions in the high-dose BLM model on day 21. The images in the lower panel are the magnifications of the dotted squared areas of the images in the upper row (a,c).

(D) The hydroxyproline content was not significantly different between the low-dose and high-dose BLM models and was significantly higher than that in control mice on day 21 (n = 6 in each group).

(E) Before administration of BLM, immunofluorescence of the lung shows lineage-positive AT2 cells in both Scgb1a1-rtTA (Line 1)/(tetO)^{7}CMV-Cre mice (upper left) and in Sftpc-CreER^{T2}/ROSA$^{mT/mG}$ mice (lower left). Twenty-one days after administration of low-dose BLM, lineage-positive AT1 cells appeared in both Scgb1a1-rtTA (Line 1)/(tetO)^{7}CMV-Cre mice (upper middle) and in Sftpc-CreER^{T2}/ROSA$^{mT/mG}$ mice (lower middle) with well-maintained alveolar structures. Lineage-negative AT2 cells accumulate in dense injured areas 21 days after high-dose BLM administration in Sftpc-CreER^{T2}/ROSA$^{mT/mG}$ mice (lower right), which were rarely observed in Scgb1a1-rtTA (Line 1)/(tetO)^{7}CMV-Cre mice (upper right).

(F) In the high-dose BLM model in Sftpc-CreER^{T2}/ROSA$^{mT/mG}$ mice, lineage-negative AT2 cells appeared on day 7. Their location at the edge of terminal bronchioles is clearly demonstrated on day 10 (areas surrounded by dotted lines). On day 21, the accumulation of lineage-negative AT2 cells progress. Their spatial association with bronchioles becomes relatively unclear because of alveolar and bronchiolar collapse and fibrosis.

(G) Representative FACS plots of the quantification of lineage-negative AT2 cells. AT2 cells were identified with surface markers (CD45$^-$CD31$^-$EpCAM^{med}MHCII$^+$), and their expression of eGFP was explored on day 7 after administration of PBS (left), low-dose BLM (middle) and high-dose BLM (right) to Sftpc-CreER^{T2}/ROSA$^{mT/mG}$ mice.

(H) The proportion of lineage-negative AT2 cells was significantly higher in the high-dose BLM model than in the PBS or low-dose BLM model on day 7 (n = 4 in each group).

(I) Quantification of total AT2 cells and Ki-67$^+$ AT2 cells in the lung during the course of BLM-induced injury and regeneration. The number of total AT2 cells significantly decreased on day 7 and did not recover thereafter through day 21. The number of proliferative AT2 cells (Ki-67$^+$ AT2 cells) peaked on day 7 and returned to close to baseline levels on day 21.

(J and K) Immunofluorescence of the lung shows that Ki-67$^+$ cells mostly appear in fibrotic areas. The distribution of AT2 cells in the nonfibrotic area was sparse compared to that at baseline. (n = 5 in day 0 and day 5, n = 4 in day 3, day 10, and day 21) k, Quantification of the number of AT2 cells shows that significant AT2 cell depletion occurs both in nonfibrotic areas and in fibrotic areas on day 10. Scale bars: 300 μm in a and c. Scale bars: 100 μm in e, f, and j. *p <0.05, **p <0.01. Data are represented as mean ± SEM in b, d, h, i, and k. The Wilcoxon rank-sum test was performed in b and i. ANOVA followed by Tukey-Kramer test was performed in d, h, and k.

areas, which was not observed in the high-dose model of Scgb1a1-rtTA/(tetO)$_7$CMV-Cre/ROSA$^{mT/mG}$ mice. These lineage-negative AT2 cells were not evident in the low-dose BLM model of either strain Figure 1E), implying that these cells are derived from club cells.

We further investigated the spatiotemporal appearance of lineage-negative AT2 cells in Sftpc-CreER^{T2}/ROSA$^{mT/mG}$ mice. These cells appeared on day 7 after high-dose BLM administration at the edge of terminal bronchioles. Their number increased over time through day 21 Figure 1F). Flow cytometric quantification revealed that 7.4 ± 1.7% (n = 4) of AT2 cells were lineage-negative in the high-dose model of Sftpc-CreER^{T2}/ROSA$^{mT/mG}$ mice on day 7, which was significantly higher than that in control mice (0.94 ± 0.04%, n = 4) or in the low-dose model (1.7 ± 0.3%, n = 4) (Figures 1G and1H).

These results suggest that in mild lung injury, AT2 cells regenerate injured AT1 cells to recover alveolar epithelial integrity and prevent alveolar collapse. However, in severe lung injury, non-AT2 cells (possibly club cells) are recruited to replenish the AT2 cell pool around the injured bronchioles (Barkauskas et al., 2013; Zheng et al., 2012).

The depleted AT2 cell pool after high-dose BLM injury does not recover despite compensatory AT2 cell proliferation

We next tried to characterize the AT2 cell number transition and their proliferative status after high-dose BLM injury (Figure 1I). A single-cell suspension of the lung was prepared, and the cell proportion was quantified by FACS. After administration of high-dose BLM, the number of AT2 cells (CD31$^-$CD45$^-$EpCAM$^+$proSP-C$^+$ cells) in the lung gradually declined and reached 54.7 ± 9.9% (n = 4) at day 10 compared to that before the treatment, which did not recover through day 21. In contrast, the number of proliferative AT2 cells (Ki-67$^+$ AT2 cells) reached a peak at day 7 but declined through day 10 and returned to baseline at day 21 Figure 1I). The immunofluorescence study on day 10 after BLM administration showed that the number of AT2 cells was decreased not only in fibrotic areas but also in nonfibrotic normal-appearing areas (n = 3 in each group) (Figures 1J and1K). These findings suggest that after severe lung injury, AT2 cells in addition to club cells actively recover alveolar epithelial cell integrity by proliferation and differentiation into AT1 cells, which is not fully compensatory, resulting in the loss of the AT2 cell pool in the fibrotic lung.
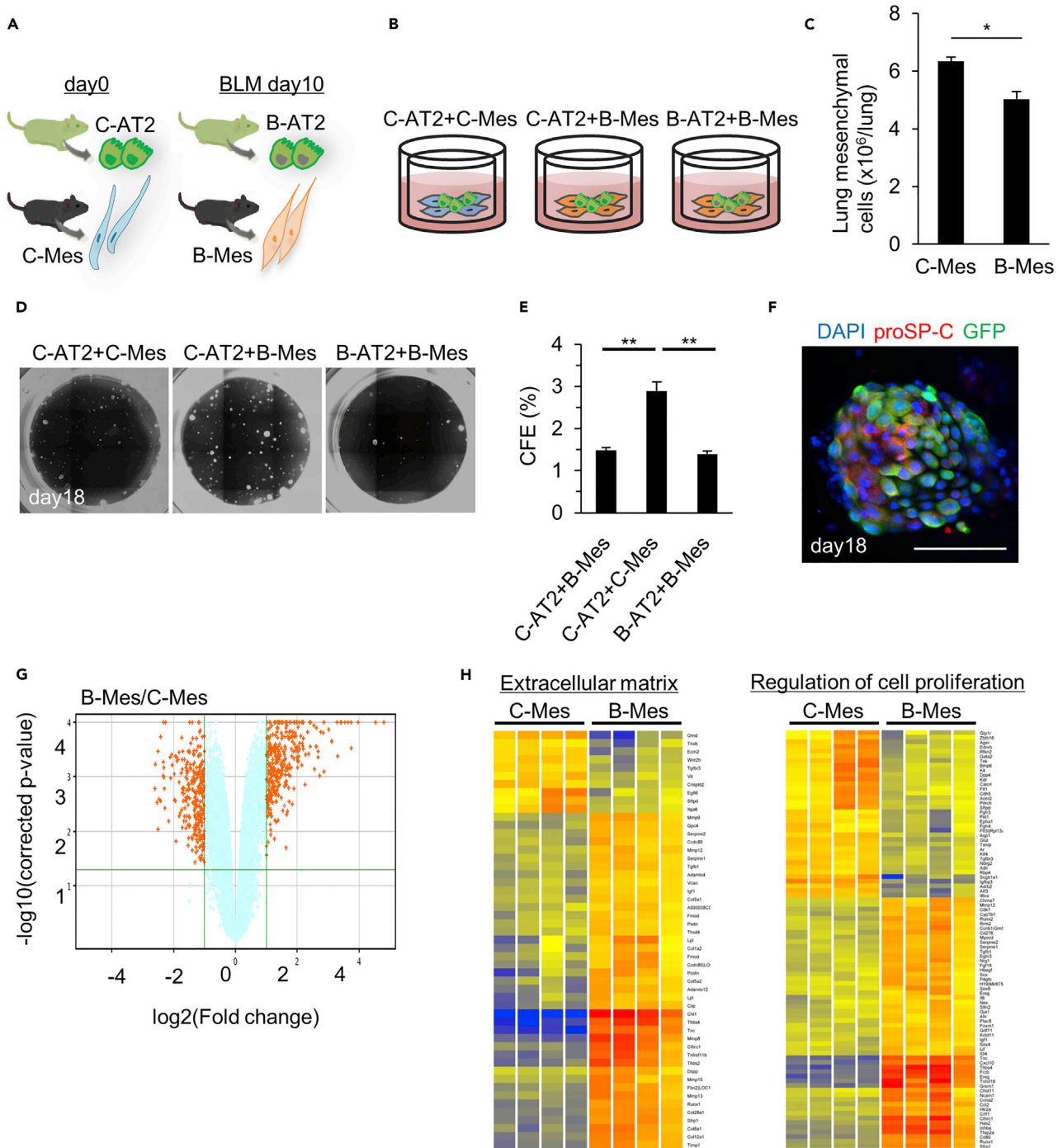
A

day0   BLM day10

C-AT2   B-AT2

C-Mes   B-Mes

B

C-AT2+C-Mes C-AT2+B-Mes B-AT2+B-Mes

C

D

C-AT2+C-Mes   C-AT2+B-Mes   B-AT2+B-Mes

day18

E

F

DAPI proSP-C GFP

day18

G

B-Mes/C-Mes

H

Extracellular matrix

Regulation of cell proliferation

C-Mes   B-Mes

C-Mes   B-Mes

Figure 2. Lung mesenchymal cells in a fibrogenic lung environment promote intact AT2 cell proliferation

(A) AT2 cells (CD45⁻CD31⁻EpCAM⁺MHCII⁺ cells) were isolated from control GFP mice (C-AT2) or high-dose BLM model GFP mice on day 10 (B-AT2). Lung mesenchymal cells (CD45⁻CD31⁻EpCAM⁻ cells) were isolated from control mice (C-Mes) or high-dose BLM model mice on day 10 (B-Mes).

(B) Schematic representation of the 3D culture of AT2 cells and lung mesenchymal cells.

(C) Quantification of lung mesenchymal cells by FACS shows that the number of B-Mes is slightly but significantly decreased compared to that of C-Mes (n = 6 in each group).

(D) Representative GFP signals in a Transwell insert show various sizes of spheres on day 18.

(E) The CFE of cultures of C-AT2 and B-fibro is 2.9% ± 0.2%, which is significantly higher than that of C-AT2 and C-Fibro (1.5% ± 0.1%) and that of B-AT2 and B-fibro (1.4% ± 0.1%) (n = 4 in each group).

Figure 2. Continued

(F) Whole-mount immunofluorescent image of a sphere in C-AT2/B-fibro co-culture on day 18 shows aggregation of proSP-C$^+$GFP$^+$ cells to form a large colony.

(G) Volcano plot showing significant differences in mRNA expression between B-Mes and C-Mes (n = 4 in each group).

(H) Heatmap plots of enriched terms identified by gene ontology analysis (n = 4 in each group). Scale bar: 100 μm *p <0.05, **p <0.001. Data are represented as mean ± SEM in c and e. The Wilcoxon rank-sum test was performed in c. ANOVA followed by Tukey-Kramer test was performed in e.

Activated lung mesenchymal cells promote AT2 cell proliferation *in vitro*

Although our data collectively showed inadequate alveolar regeneration by AT2 cells in fibrotic lungs, it is unknown whether this is attributed to the injury of AT2 cells themselves or the resultant activation of mesenchymal cells and the creation of a microenvironment that could inhibit AT2 cell regeneration.

To examine the association between activated lung mesenchymal cells and AT2 cell proliferation after BLM treatment, we utilized AT2 cell-mesenchymal cell organoid assays. Isolated control AT2 cells from GFP mice (C-AT2) were cultured with lung mesenchymal cells from BLM-injured lungs (B-Mes) or control lungs (C-Mes) to assess the colony-forming efficacy (CFE) of AT2 cells. We also isolated AT2 cells from BLM-injured lungs (B-AT2) and cultured them with B-Mes (Figures 2A and 2B). B-Mes/B-AT2 and C-Mes/C-AT2 were isolated 10 days after administration of high-dose BLM or PBS, when the transition from the inflammatory phase to the fibrotic phase occurred in the BLM model (Moeller et al., 2008). The number of B-Mes quantified by FACS showed a modest but statistically significant decrease compared to that of C-Mes (Figure 2C), indicating phenotypic changes, not numerical increases, in resident mesenchymal cells in pulmonary fibrosis (Tsukui et al., 2013). Organoid assays revealed that the CFE of C-AT2 cultured with B-Mes was significantly higher than that of C-AT2 cultured with C-Mes, while the CFE of B-AT2 cultured with B-Mes was significantly lower than that of C-AT2 cultured with B-Mes (Figures 2D and 2E). Immunofluorescence showed that proSP-C$^+$ AT2 cells aggregated to form large colonies in the C-AT2/B-Mes coculture (Figure 2F). These results indicate that lung mesenchymal cells are activated in injured lungs to create a microenvironment that promotes the proliferation of AT2 cells. At the same time, importantly, endogenous AT2 cells in the BLM model responded poorly to these conditions that favor cell proliferation.

To further explore the phenotypic changes in lung mesenchymal cells after BLM injury, we next performed microarray analysis on C-Mes and B-Mes Figure 2G). Microarray analyses identified 352 genes that were significantly upregulated more than 2-fold in B-Mes compared to C-Mes. The 20 transcripts that were upregulated most in B-Mes are listed in Table 1, which includes important genes for pulmonary fibrosis, such as *Spp1* (Berman et al., 2004), *Tenascin C* (Carey et al., 2010), and *Mmp8* (Garcia-Prieto et al., 2010). Upregulation of these genes indicates the profibrotic properties of B-Mes. To further elucidate the functional significance of the transcriptional changes in B-Mes, we assessed GO term enrichment. The GO terms that were the most enriched in the upregulated genes were "Extracellular region part" followed by "Extracellular region", "Extracellular space", and "Extracellular matrix", as expected. Of interest, the GO term "Regulation of cell proliferation" was also identified in B-Mes, implying the contribution of B-Mes to epithelial cell proliferation in fibrotic lungs (Figure 2H).

Exogenously transplanted AT2 cells successfully reconstitute alveolar structures in fibrotic lungs and compensate for the local loss of AT2 cells

Next, to prove the interaction of B-Mes *in vivo* with intact AT2 cells (C-AT2), we intratracheally transplanted freshly isolated murine AT2 cells into the lungs 10 days after high-dose BLM administration and explored their fate thereafter. For transplantation, GFP$^+$ AT2 cells were isolated from GFP mice for identification of transplanted cells and their progeny (Figure 3A). AT2 cells did not engraft in PBS-administered control lungs when evaluated at 11 days post transplantation (dpt). At 11 dpt, flow cytometric analyses of the BLM-injured lungs transplanted with GFP$^+$ AT2 cells revealed that 1.9 ± 0.1% (n = 4) of CD45$^-$CD31$^-$EpCAM$^+$ cells were positive for GFP expression Figure 3B). Immunofluorescence of cytospin preparations of sorted CD45$^-$CD31$^-$EpCAM$^+$GFP$^+$ cells demonstrated both proSP-C$^+$ AT2 cells and AQP5$^+$ AT1 cells Figure 3C), suggesting successful engraftment and differentiation of transplanted AT2 cells in BLM-injured lungs. We next performed time course analyses of transplanted cells by immunofluorescence. At 3 dpt, GFP$^+$ AT2 cells engrafted as small cell clusters adjacent to active fibrotic areas Figure 3D). At 7 dpt, with expansion of the colony size (Figure 3E), GFP$^+$ AT1 cells were observed (Figure 3F). At 11 dpt (BLM day 21), engrafted AT2 cells formed alveolar epithelial cell colonies containing both AT1 and AT2 cells mostly adjacent to fibrotic areas (Figure 3G). AT2 cells positive for Ki-67 expression also existed in the colonies (Figure 3H), suggesting that colony expansion was still underway in this phase. Other than colonies adjacent to the fibrotic areas, there were two other colony formation patterns in the lungs. One pattern was small colonies showing neither cellular proliferation nor differentiation into AT1 cells in the center

Table 1. The 20 most upregulated genes in lung mesenchymal cells at 10 days after BLM treatment

Symbol	Fold change	p-value
Spp1	28.0	3.11E-05
Chl1	23.3	2.04E-05
Rgs16	15.7	1.11E-05
Cxcl13	13.4	2.98E-04
P4ha3	13.4	9.03E-05
Thbs4	12.6	7.44E-05
Fst	11.6	3.33E-05
Frzb	10.7	2.53E-05
Ereg	10.6	2.56E-05
Tnfsf18	9.9	4.33E-04
Tnc	9.7	5.99E-06
Mmp8	8.7	2.25E-04
Grem1	8.7	2.28E-04
Saa3	8.1	1.40E-04
Ltbp2	7.3	3.56E-05
9930013L23Rik	7.3	8.12E-04
Cxcl10	7.2	2.04E-05
Tfap2a	7.2	1.59E-04
Inhba	6.8	1.51E-04
Fgf23	6.6	9.74E-04

of fibrotic areas. These cells were also negative for fibroblast markers, such as desmin and αSMA (Figure 3I), not supporting epithelial-mesenchymal transition. The other was a few small alveolar-like colonies in normal-appearing areas where no αSMA$^+$ myofibroblasts existed (Figure 3J).

To elucidate the spatial distribution of regenerated areas by endogenous AT2 cells, endogenous non-AT2 cells (club cells), and exogenously transplanted AT2 cells, we intratracheally transplanted GFP$^+$ AT2 cells from GFP mice to Sftpc-CreER^{T2}/ROSA$^{mT/mG}$ mice on day 10 of high-dose BLM treatment. Endogenous AT2 cells were labeled with membranous GFP expression (mGFP-AT2) and were distinguished from exogenous transplanted AT2 cells with nuclear and cytoplasmic GFP expression (ncGFP-AT2) (Figure S2A). At 11 dpt, exogenous transplanted AT2 cells (ncGFP-AT2) engrafted and formed alveolar epithelial colonies (Figures S2B and S2C), which were in close proximity to fibrotic areas and surrounded by AT2 cells with no GFP expression (endogenous AT2 cells differentiated from non-AT2 cells). These areas were demarcated from areas regenerated by endogenous AT2 cells (mGFP-AT2) (Figures S2B and S2D), suggesting a locally complementary effect of AT2 cell transplantation.

AT2 cell transplantation ameliorates BLM-induced lung fibrosis, regenerates alveolar structures and recovers lung function

We evaluated AT2 cell-transplanted models not only in the acute phase (11 dpt, BLM day 21) but also in the chronic phase (90 dpt, BLM day 100). In the histological evaluation at 90 dpt, cell-rich dense fibrotic areas resolved, which left band-like fibrotic areas in AT2 cell-transplanted mice (Figure 3K). Immunofluorescence revealed alveolar-like colonies derived from exogenous AT2 cells mostly at the edge of the fibrotic areas. αSMA$^+$ myofibroblasts disappeared in both AT2 cell-transplanted and nontransplanted mice on day 100 of BLM administration (Figure 3L). A hydroxyproline assay showed that AT2 cell transplantation did not significantly reduce collagen accumulation at 11 dpt (Figure 3M). At 90 dpt, however, a significant reduction in the hydroxyproline content was observed in AT2 cell-transplanted mice (Figure 3N). Likewise, static lung compliance in AT2 cell-transplanted mice was significantly improved compared to that in nontransplanted mice at 90 dpt (Figure 3O). The mRNA expression levels of both Col1a1 and Col3a1 in whole lung lysates were not significantly different between AT2 cell-transplanted and nontransplanted BLM-injured mice at either 11 dpt or 90 dpt (Figure S3A). Furthermore, Col1a1 and Col3a1 expression was not significantly different between control and BLM-injured mice on
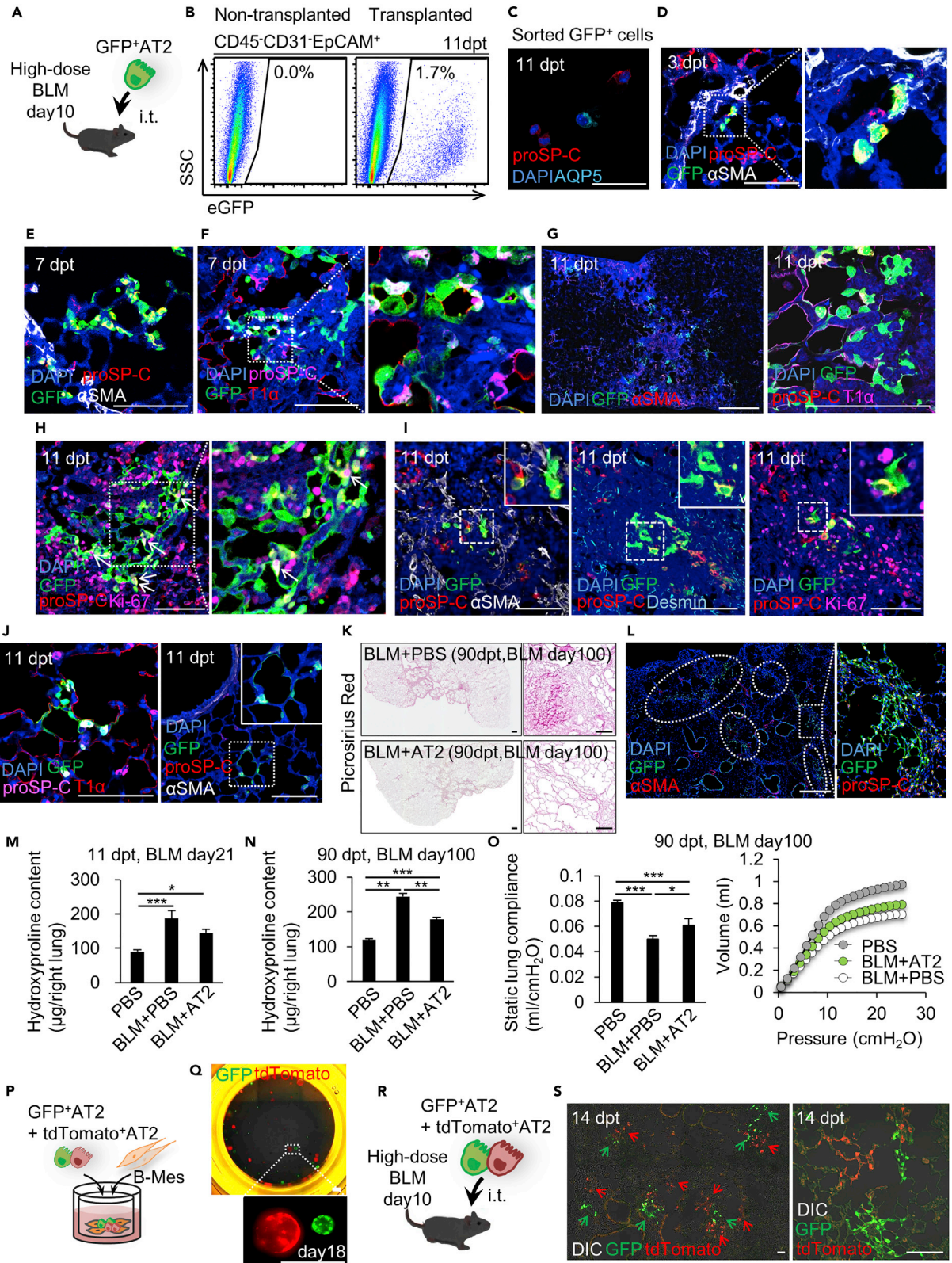
Figure 3. AT2 cell transplantation reconstitutes alveolar structure to ameliorate bleomycin-induced lung fibrosis

(A) Schematic representation of AT2 cell transplantation in high-dose BLM model mice. AT2 cells were freshly isolated from C57BL/6-Tg(CAG-EGFP) mice, resuspended in a volume of 100 μL of PBS, and intratracheally transplanted to high-dose BLM model mice on day 10 (C57BL/6J).

(B) Representative FACS plots of the reanalysis of nontransplanted mice (left) and AT2 cell-transplanted mice (right) 11 days after transplantation (dpt) (day 21 of the high-dose BLM model). Mouse lungs were dissociated and analyzed for GFP expression with surface markers. A total of 1.9% $\pm$ 0.1% of $CD45^-CD31^-EpCAM^+$ cells were positive for GFP expression (n = 4).

(C) Cytospin preparations of sorted $CD45^-CD31^-EpCAM^+GFP^+$ cells show a mixture of $proSP^-C^+$ cells and $AQP5^+$ cells.

(D) At 3 dpt, a few GFP^+ AT2 cell clusters were observed.

(E and F) At 7 dpt, the colony sizes are enlarged at the edge of the active fibrotic areas, where αSMA^+ myofibroblasts are present. Some GFP^+ cells express T1α, an AT1 cell marker.

(G) At 11 dpt, a low-magnification image shows that multiple GFP-positive colonies are formed mostly at the edge of fibrotic areas (left panel). A representative GFP-positive colony at 11 dpt shows that some GFP^+ cells differentiate into AT1 cells, which cover the inner surface of aerated areas (right panel).

(H) Around engrafted GFP^+ colonies, infiltration of $Ki-67^+$ cells was observed. Some GFP^+ cells were also positive for Ki-67 expression (arrows).

(I) Within fibrotic areas, small colonies of engrafted AT2 cells are present. These cells are surrounded by fibroblasts but are negative for fibroblast markers themselves, such as αSMA (left) and desmin (central). Engrafted cells are negative for Ki-67 expression, although multiple $Ki-67^+$ cells are infiltrated (right).

(J) Other colony formation patterns include small alveolar-like colonies in normal-appearing areas (left panel), where BLM-induced myofibroblasts are absent (right panel).

(K) Low-magnification (left panels) and high-magnification (right panels) images of picrosirius red staining show more collagen deposition in control high-dose BLM model mice (upper panels) than in AT2 cell-transplanted high-dose BLM model mice (lower panels) at 90 dpt.

(L) A low-magnification image of AT2 cell-transplanted high-dose BLM model mice at 90 dpt shows multiple GFP^+ colonies at the edge of band-like fibrosis areas (areas surrounded by dotted lines). Note that the αSMA^+ myofibroblasts disappeared. An enlarged view of a GFP^+ colony shows an alveolar-like structure formed by engrafted GFP^+ cells (right panel).

(M) At 11 dpt, the hydroxyproline content of the lung was not significantly different between nontransplanted high-dose BLM model mice and AT2 cell-transplanted high-dose BLM model mice (n = 7 in BLM + PBS group, n = 8 in PBS group and BLM + AT2 group).

(N) At 90 dpt, the hydroxyproline content of the lung in AT2 cell-transplanted high-dose BLM model mice significantly decreased compared to that of nontransplanted high-dose BLM model mice (n = 8 in PBS group, n = 6 in BLM + PBS group, n = 7 in BLM + AT2 group). Note that both nontransplanted and AT2 cell-transplanted high-dose BLM model mice showed higher hydroxyproline contents in the lungs than control mice on day 100 of BLM administration.

(O) The static compliance of the lung in AT2 cell-transplanted mice was significantly higher than that in nontransplanted mice (n = 8 in PBS group. n = 6 in BLM + PBS group, n = 7 in BLM + AT2 group).

(P) The same number (2.5×10^3 cells) of freshly isolated AT2 cells from C57BL/6-Tg(CAG-EGFP) mice and ROSA$^{mT/mG}$ mice were mixed and cultured with lung mesenchymal cells isolated from high-dose BLM model mice (C57BL/6J mice) on day 10 in a 24-well Transwell insert.

(Q) The GFP and tdTomato signals in a Transwell insert show that multiple colonies formed with either GFP or tdTomato protein expression on day 18.

(R) The same number (2×10^5 cells) of freshly isolated AT2 cells from C57BL/6-Tg(CAG-EGFP) mice and ROSA$^{mT/mG}$ mice were mixed and intratracheally administered to high-dose BLM model mice (C57BL/6J mice) on day 10.

(S) At 14 dpt, immunofluorescence shows multiple colonies with mutually exclusive fluorescent protein expression. Scale bar: 50 μm in c, Scale bars: 100 μm in a, d, e, f, g (right), h, i, j, and k (right); and s. Scale bars: 500 μm in k (left), l (left) and q. Scale bar: 1000 μm in g (left). *p <0.05, **p <0.01, ***p <0.001. Data are represented as mean $\pm$ SEM in m, n and o. ANOVA followed by Tukey-Kramer test was performed in m, n, and o.

BLM day 100, suggesting that the level of collagen synthesis declines to normal levels in this phase of the BLM model (Figure S3B).

Activated lung mesenchymal cells allow the formation of monoclonal colonies by AT2 cells both *in vitro* and *in vivo*

Clonal proliferation of AT2 cells was demonstrated after AT2 cell-targeted depletion *in vivo* (Barkauskas et al., 2013). To elucidate the mode of formation of alveolar epithelial cell colonies in our model, we utilized AT2 cells expressing two different fluorescent proteins to assess monoclonal expansion. The same number of GFP^+ AT2 cells from GFP mice and tdTomato$^+$ AT2 cells (2.5×10^3 cells of each) from ROSA$^{mT/mG}$ mice were mixed and cultured with B-Mes (Figure 3P). Colonies formed in this co-culture exhibited only fluorescent protein expression (Figure 3Q), supporting the monoclonality of the alveolar epithelial colonies promoted by activated lung mesenchymal cells *in vitro*. In the same way, transplantation of mixed GFP^+ AT2 cells and tdTomato$^+$ AT2 cells (2×10^5 cells of each) into BLM-injured lungs (Figure 3R) demonstrated that each alveolar epithelial cell colony expressed mutually exclusive fluorescent proteins (Figure 3S). These results revealed the capacity of single intact AT2 cells to form alveolar epithelial colonies in severely injured lungs to promote alveolar regeneration.

Exogenously transplanted lung mesenchymal cells are engrafted and activated within fibrotic areas

The lung fibrogenic microenvironment is appropriate for AT2 cell proliferation and promotes alveolar regeneration by intact AT2 cells. To further characterize this microenvironment, other cellular components of the lungs were also transplanted. C-Mes intratracheally transplanted on day 10 of high-dose BLM injury (Figure S4A)
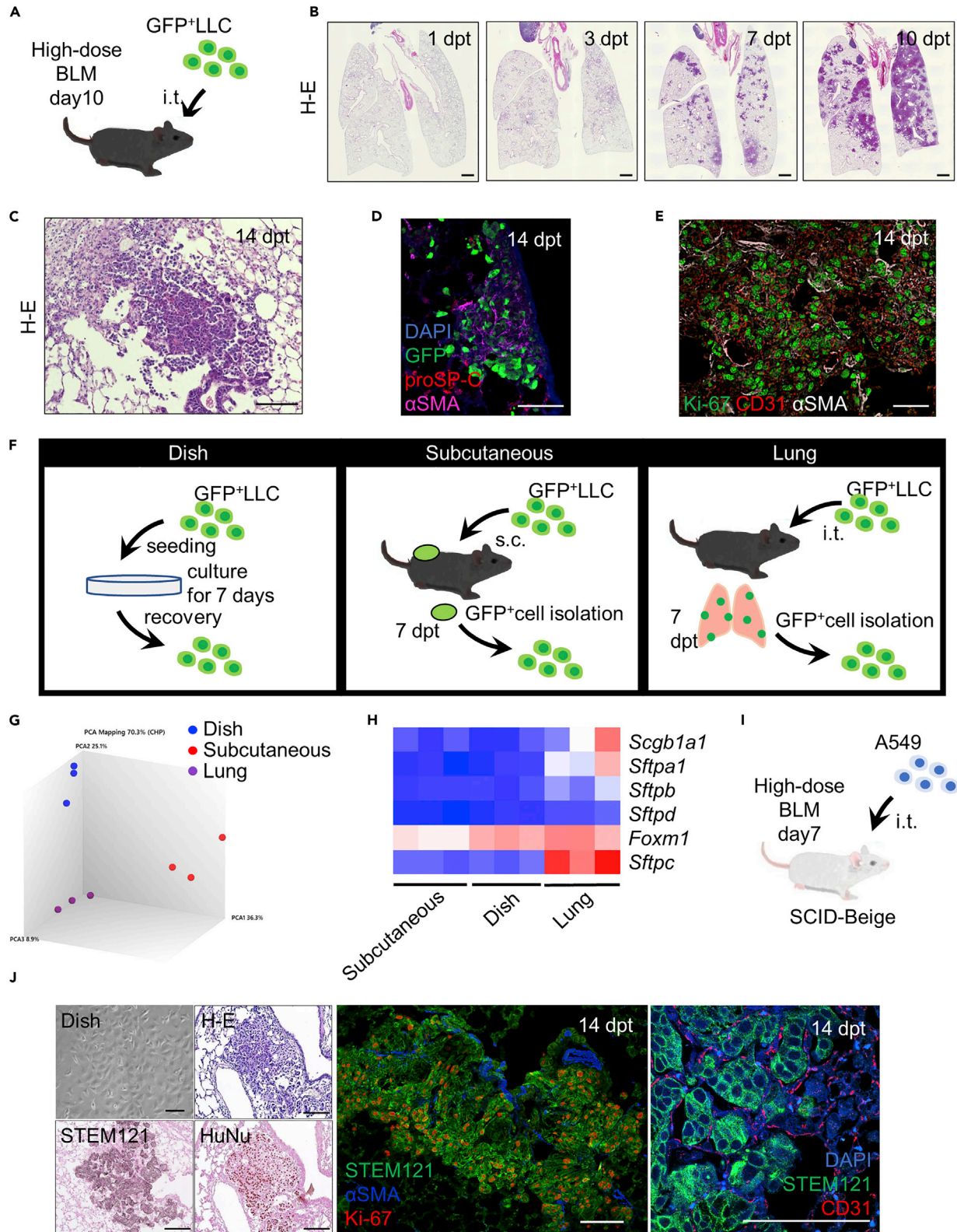
Figure 4. A novel orthotopic lung cancer model shows relevant tumor formation with lung-specific gene expression in tumor cells

(A) Schematic of the orthotopic lung cancer model. Ten days after intratracheal instillation of 2 mg/kg bleomycin (BLM) to 8- to 10-week-old C57BL/6 mice, 4×10^5 GFP-labeled Lewis lung carcinoma (GFP$^+$ LLC) cells were intratracheally transplanted.

(B) Representative histological findings of H–E staining of the lungs from mice sacrificed at 1, 3, 7, and 10 dpt.

(C) Representative histological findings of H–E staining at 14 dpt. Tumor nests were localized at bronchoalveolar transition regions with BLM-induced fibrosis and consisted of tumor cells and stromal cells. Scale bar: 100μm.

(D) Immunofluorescence analysis at 14 dpt. GFP$^+$ colony formulation and αSMA$^+$ spindle cells were observed in the tumor nest. Scale bar: 100 μm.

(E) Representative immunofluorescence of Ki-67, αSMA, and CD31 at 14 dpt. Scale bar: 100 μm.

(F) Schematic of the microarray analysis and analysis of the gene expression profiles of GFP$^+$ LLC cells grown in 2-dimensional monolayer culture, subcutaneous tumors, and tumors in BLM-injured lungs.

(G) Principal component analysis among three types of isolated cells (n = 3 in each group).

(H) The expression patterns of lung-specific genes (n = 3 in each group).

(I) Schematic of the orthotopic lung cancer model. Seven days after intratracheal instillation of 3 mg/kg BLM to 8- to 10-week-old CB17.Cg-PrkdcscidLystbg-J/CrlCrlj mice, A549 cells (1×10^5 cells to 4×10^5 cells), were intratracheally transplanted.

(J) Representative histological findings at 14 dpt. Immunohistochemistry showed that the tumor nest was positive for human-specific antibodies (STEM 121 antibody and anti-human nuclear antigen (HuNu) antibody). In immunofluorescence analysis, STEM121$^+$ and Ki-67$^+$ colony formations and αSMA$^+$ spindle cells were observed in the tumor nest. Furthermore, tumor cells were positive for STEM121, and stromal cells were positive for CD31. Scale bar: 1000 μm in b, Scale bars: 100 μm in c, d, e and j.

engrafted around fibrotic areas, and some expressed αSMA at 3 dpt (Figure S4B). At 11 dpt, most of the engrafted cells expressed αSMA and formed myofibroblast colonies surrounded by endogenously emerged myofibroblasts within fibrotic areas (Figure S4B). Endothelial cells (CD45$^-$CD31$^+$EpCAM$^-$ cells) transplanted in the same way did not engraft when evaluated at 11 dpt. These results suggest that the lung fibrogenic microenvironment not only promotes alveolar epithelial regeneration but also activates mesenchymal cells, promoting fibrosis as previously described (Tsukui et al., 2015).

Murine lung cancer cells generate multiple tumor nests in the BLM model

Next, we evaluated the lung cancer cell dynamics in the lung fibrogenic microenvironment. The LLC cells, a murine lung cancer cell line established from C57BL/6 mice, were intratracheally administered to control mice or BLM model mice (Figure 4A). LLC cells did not engraft in PBS-administered control lungs, whereas in the BLM model, LLC cells generated multiple tumor nests, and their size increased over time after transplantation Figure 4B. Tumor nests were relatively localized at the edge of bronchioles with BLM-induced fibrosis (Figure 4C), where αSMA$^+$ myofibroblasts exist Figure 4D. Ki-67$^+$ tumor cells were interspersed with endogenous myofibroblasts and endothelial cells to form tumor nests (Figure 4E). Then, we evaluated the tumor generation efficiency and the tumor cell passage potential in vivo. Multiple tumor nests were generated, even with just 1×10^2 cells as we decreased the number of LLC cells to transplant (Figure S5). The engrafted GFP-labeled LLC cells were successfully isolated and generated tumor nests again in murine lungs (Figure S6A). Cell viability quantified by FACS at passages 0 (n = 5), 1 (n = 5) and 2 (n = 3) was 88.2 $\pm$ 1.1%, 86.7 $\pm$ 1.8% and 88.6 $\pm$ 0.6%, respectively (Figure S6B). The proportions of LLC cells (CD31$^-$CD45$^-$GFP$^+$ cells) in the single-cell suspension at 7 dpt at passages 0, 1 and 2 were 5.9 $\pm$ 3.9%, 44.5 $\pm$ 5.6% and 23.1 $\pm$ 7.0%, respectively (Figure S6C). The histological appearances of tumor nests at passage 0 and passage 2 were unchanged (Figure S6D). These findings demonstrated that the lung fibrogenic microenvironment also provides room for tumor cell engraftment and proliferation with high efficiency. Of note, transplanted tumor cells autonomously encompassed endogenous cells to form tumor nests, possibly creating the optimal microenvironment for their survival.

LLC cells in the lung model express lung-specific genes compared to subcutaneous engraftment cells

Next, we hypothesized that tumor cells in the lungs are differently influenced by their unique lung fibrogenic microenvironment compared to those in subcutaneous tumor models in vivo or in 2-dimensional monolayer culture in vitro. We conducted microarray analysis and analyzed the gene expression profiles of LLC cells grown in 2-dimensional monolayer culture, in subcutaneous models (subcutaneous tumors), and in BLM lungs (lung tumors) (Figures 4F and S7A). Principal component analysis (PCA) results displayed clear differences in the transcriptional profiles among the three groups (Figure 4G). The expression patterns of lung-specific genes, such as *Scgb1a1, Sftpa1, Sftpb, Sftpc, Sftpd,* and *Foxm1,* were altered mainly in lung tumors (Figure 4H). *Sftpc* was the most upregulated gene in lung tumors, and its protein product, proSP-C, was positive in lung tumors by immunohistochemistry but negative in subcutaneous tumors (Figure S7B). In total, 1,928 genes were upregulated in lung tumors compared to subcutaneous tumors, whereas 1,103 genes were downregulated in lung tumors. GO enrichment analysis of the differentially expressed genes (DE-Gs) between subcutaneous tumors and lung

Table 2. GO functional enrichment analysis of up- and downregulated DE-Gs (top five in each)

Items		Term	Description	Count	FDR
Upregulated	Enrichment score: 18.0	GO:0007049	cell cycle	137	8.13E-20
		GO:0051301	cell division	86	3.95E-12
		GO:0007067	mitotic nuclear division	68	1.68E-10
	Enrichment score: 11.7	GO:0005739	mitochondrion	238	1.03E-08
	Enrichment score: 11.6	GO:0008380	RNA splicing	66	1.45E-12
Downregulated	Enrichment score: 5.3	GO:0016126	sterol biosynthetic process	12	4.27E-05
		GO:0006694	steroid biosynthetic process	15	0.002
		GO:0006629	lipid metabolic process	46	0.015
		GO:0008202	steroid metabolic process	16	0.023
		GO:0006695	cholesterol biosynthetic process	10	0.029

PDX, patient-derived xenograft; ADC, adenocarcinoma; LCNEC, large cell neuroendocrine carcinoma; TNM, TNM classification based on the eighth edition of the Union for International Cancer Control classification; M, male; F, female.

tumors suggested altered gene functions, including 143 GO terms for genes that are highly expressed in lung tumors and 61 GO terms for those in subcutaneous tumors (Table 2). The most significantly enriched GO function for genes highly expressed in lung tumors was regulation of the cell cycle, and that for the downregulated genes was steroid biosynthetic process.

Orthotopic xenograft models of human lung cancer cell lines are relevant to pharmacological intervention

Lung epithelial cell-specific gene expression by LLC cells in the BLM model implied that our novel orthotopic xenograft model could be more relevant in terms of the pathobiology of lung cancer. Thus, we applied human lung cancer cell lines to this model using CB17.Cg-Prkdc^{scid}Lyst^{bg-J}/CrlCrlj (SCID-Beige) mice (Helene et al., 1999; Tang et al., 2014) (Figure 4I). Intratracheally transplanted A549 cells generated tumor nests containing endogenous αSMA$^+$ myofibroblasts and CD31$^+$ endothelial cells (Figure 4J), similar to the LLC cell models. Other human non-small cell lung cancer (NSCLC) cell lines, such as adenocarcinoma (H441; n = 4, PC9; n = 2, and H1975; n = 2), squamous cell carcinoma (H226: n = 4), and large cell carcinoma (H460: n = 2 and H1299: n = 4), were also applied (Figure S8). Immunohistochemistry of the STEM121 antigen and anti-human nuclear antigen enabled the differentiation of human cancer cells from endogenous murine cells. The engraftment rate was 100%. There was no evidence of extrapleural metastasis or pleural effusion in any cell lines. The histological appearances of lung tumors derived from each cell line were similar to those in culture dishes. The proliferative rate in the lungs was different among cell lines and mostly reflected that in the 2-dimensional monolayer culture.

Next, we attempted to elucidate the feasibility of our orthotopic xenograft model for pharmacological intervention. Orthotopic xenograft models created by PC-9 cells, which harbor an epidermal growth factor receptor (EGFR)-activating gene mutation, exon 19 deletion, were treated with gefitinib, an EGFR tyrosine kinase inhibitor (Figure 5A). In our preliminary experiment, 2 weeks of incubation after intratracheal transplantation of PC9 cells led to pulmonary nodules large enough to be evaluated using computed tomography (CT). Two weeks of gefitinib treatment starting from 14 dpt (Cross et al., 2014; Taguchi et al., 2004) induced significant tumor shrinkage represented by a nearly 99% reduction in tumor volume evaluated by three-dimensional computed tomography (3D-CT) volumetry Figure 5B. Histological evaluation also demonstrated a significant effect of gefitinib on lung cancer formed by transplanted PC-9 cells in BLM-injured lungs.

Human lung cancer cells and AT2 cells can form tissue structures in BLM models to establish L-PDXs or pulmonary alveolar regeneration methods

We applied our orthotopic xenograft model using human primary cells to establish an L-PDX or pulmonary alveolar regeneration method in precision medicine Figure 5C. For L-PDX, we intratracheally administered a cell suspension of surgically resected tumors to the BLM model of SCID-Beige mice. The viability of cells
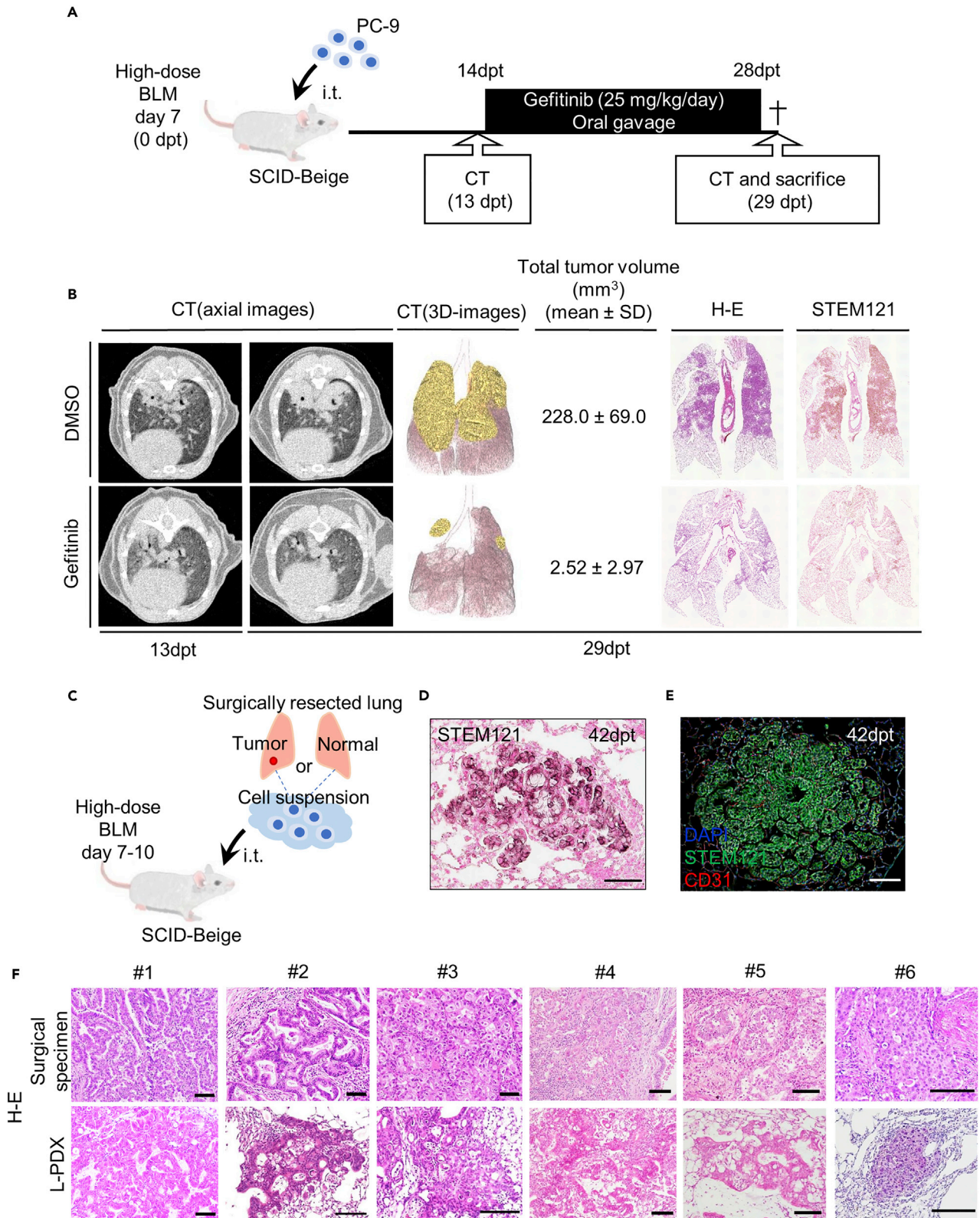
A

B

C

D

E

F

Figure 5. Orthotopic xenograft models are relevant to pharmacological intervention to establish L-PDXs for clinical application

(A) Protocol for the gefitinib treatment of a xenograft model using PC-9 cells harboring an epidermal growth factor receptor exon 19 deletion.

(B) Computed tomography (CT) images of pre- and post-gefitinib treatment and images of 3-dimensional reconstruction of CT images (3D-CT), H-E and immunohistochemistry (STEM121) staining at 15 days after gefitinib treatment. Tumor volume evaluation via 3D-CT volumetry (n = 5 in each group).

(C) Schematic of the exploratory experiments to establish orthotopic lung patient-derived xenografts (L-PDXs) or pulmonary alveolar regeneration techniques. Seven to 10 days after intratracheal instillation of 3 mg/kg BLM to 8- to 10-week-old CB17.Cg-PrkdcscidLystbg-J/CrlCrlj mice, cell suspensions derived from surgically resected tumors ranging from 1×10^5 - 1×10^6 cells or 1×10^6 cells of cell suspension derived from surgically resected lung tissue were intratracheally transplanted.

(D–F) Tumor cells were positive for STEM121 antigen. Scale bar: 100 μm.

(E) Immunofluorescence analysis showed that tumor stromal cells were positive for CD31 and αSMA and negative for STEM121. Scale bar: 100 μm.

(F) Representative H-E staining findings of tumors in the L-PDX. Scale bar: 100 μm. Data are represented as mean ± SD in b. The Wilcoxon rank-sum test was performed in b.

from resected tumors was more than 90% after preparation of a single-cell suspension. STEM121$^+$ tumor nests were generated (Figure 5D), which included endogenous tumor stromal cells Figure 5E). The engraftment rate was 77.8% (7/9) (Figure5F). All patient characteristics are shown in Table 3. The histological types of 2 failed cases were minimally invasive adenocarcinoma and lymphoepithelioma-like carcinoma. A single-cell suspension derived from surgically resected normal lung tissue distal enough to the cancer region was also intratracheally administered. STEM121$^+$ alveolar-like structures were formed (Figure S9A). Isolated human AT2 cells from surgically resected lung tissue showed STEM121$^+$ cells forming alveolar structures, some of which were also positive for proSP-C, demonstrating successful engraftment and tissue reconstitution by primary human AT2 cells in the lung fibrogenic microenvironment (Figure S9B).

DISCUSSION

Mesenchymal cell activation, a hallmark of pulmonary fibrosis, has drawn attention in terms of progressive fibrinogenesis and is a target of therapeutic intervention. Although growing evidence suggests the importance of AT2 cell damage in the development of pulmonary fibrosis, the dynamics of AT2 cells in the lung fibrogenic microenvironment have not been fully elucidated. Our data provide a comprehensive understanding of AT2 cell behavior in fibrotic lungs, and the results demonstrate both quantitative and qualitative deficits in AT2 cells. On the basis of the interaction between activated mesenchymal cells and intact AT2 cells, AT2 cell transplantation facilitated alveolar regeneration by autonomous tissue reconstruction in the lung fibrogenic microenvironment, where lung cancer cells also formed tumor nests to establish an orthotopic xenograft model.

One new observation reported here is that exogenously administered intact AT2 cells have the capacity for monoclonal expansion *in vivo* in response to the lung fibrogenic microenvironment. Furthermore, three engraftment patterns of AT2 cells represent microenvironmental heterogeneity of fibrotic lungs, by which the mode of autonomous alveolar epithelial reconstitution is influenced. Barkauskas et al. reported that endogenous AT2 cells have the capacity for clonal expansion after diphtheria toxin-mediated ablation of AT2 cells *in vivo* (Barkauskas et al., 2013). We extended the knowledge in this area by demonstrating that exogenously transplanted AT2 cells also undergo monoclonal expansion and, in part, differentiate into AT1 cells to reconstitute alveolar structures in fibrotic lungs. Furthermore, this autonomous tissue reconstitution is not limited to AT2 cells. Both lung mesenchymal cells and lung cancer cells can reproduce their own tissue phenotype together with various types of endogenous cells activated by BLM injury.

In particular, we elucidated that the lung fibrogenic microenvironment confers more relevant tumor formation properties to lung cancer cells. In contrast to LLC subcutaneous models, where homogeneous single nests of transplanted cell-oriented tumors were formed, tumor nests in LLC-BLM models formed together with endogenous mesenchymal and endothelial cells, autonomously creating a tumor microenvironment. Furthermore, compared to tumor cells in the subcutaneous transplantation model, tumor cells in the orthotopic transplantation model express alveolar epithelial cell-specific genes, such as surfactant protein genes. Similar to intrinsic tumor cell formation, the growth of exogenous tumor cells is affected by the surrounding microenvironment. This means that an inappropriate locus of transplantation may result in misleading results (Bankert et al., 2002; Bibby, 2004; Chijiwa et al., 2015). Histological similarities between surgically resected original tissues and L-PDX support the notion that our orthotopic xenograft model recapitulates the original tumor features well.

It is noteworthy that AT2 cell transplantation improved lung function in the chronic phase of the BLM model, suggesting a long-lasting effect of exogenous AT2 cells in fibrotic lungs. This finding is supported

Table 3. Patient characteristics of orthotopic lung patient-derived xenografts

	Age	Sex	Histology	Histological subtype of ADC	TNM	Transplanted cell count (cells)
#1	75	M	ADC	Micropapillary predominant	T1cN2M0	1×10^5
#2	45	F	ADC	Papillary predominant	T2aN0M0	1×10^6
#3	74	M	ADC	Papillary predominant	T1bN0M0	1×10^6
#4	56	M	ADC	Papillary predominant	T1aN0M0	1×10^6
#5	64	M	ADC	Lepidic predominant	T1bN0M0	1×10^6
#6	51	M	ADC + LCNEC	Solid predominant	T2aN2M0	1×10^5
Succeeded	70	F	ADC	Papillary predominant	T1aN0M0	1×10^6
Failed	71	F	ADC	Invasive mucinous adenocarcinoma	T1bN0M0	1×10^6
Failed	64	M	Lymphoepithelioma-like carcinoma		T1cN1M0	1×10^6

PDX, patient-derived xenograft; ADC, adenocarcinoma; LCNEC, large cell neuroendocrine carcinoma; TNM, TNM classification based on the eighth edition of the Union for International Cancer Control classification; M, male; F, female.

by the fact that exogenous cells maintained their alveolar-like colonies not only at the acute phase (21 dpt) but also at the chronic phase (90 dpt) of theBLM model. The lung fibrogenic microenvironment changes over time. In the chronic phase of the BLM model, whereas the level of collagen production returns to that in a steady state, the total collagen content in the lungs is still increased compared to the control, which might mimic human stable pulmonary fibrosis.

There are several potential mechanisms to explain the effect of AT2 cell transplantation in fibrotic lungs. First, transplanted AT2 cells compensate for the loss of endogenous AT2 cells quantitatively by forming alveolar epithelial colonies. It has been demonstrated that increasing the number of AT2 cells prior to injury is protective against acute lung injury. Pretreatment with keratinocyte growth factor (KGF), a growth factor of AT2 cells, induces AT2 cell proliferation and ameliorates hyperoxia-induced lung injury (Panos et al., 1995) or BLM-induced lung injury in rats (Yi et al., 1996). Second, the formation of alveolar epithelial colonies may help to maintain the epithelial barrier and alveolar structures. Together with this structural reconstitution, the secretion of pulmonary surfactant by AT2 cells (Mulugeta et al., 2015) also prevents alveolar collapse, which then prevents the progression of pulmonary fibrosis (Moeller et al., 2008). Third, engrafted AT2 cells may modulate fibroblast function. AT2 cells were demonstrated to produce prostaglandin E2 (PGE2) and to suppress the proliferation of fibroblasts (Lama et al., 2002). The level of PGE2 is reportedly decreased in the epithelial lining fluid of patients with idiopathic pulmonary fibrosis (Borok et al., 1991).

In conclusion, we elucidated the processes involved in exogenous cell-specific autonomous tissue construction in a lung fibrogenic microenvironment. Taking advantage of this information, AT2 cell transplantation and orthotopic lung cancer models would be promising for epithelial cell-targeted therapy in fibrotic lung disease and precision medicine in lung cancer.

Limitations of the study

Our study has some limitations. First, we cannot identify specific mesenchymal cells or humoral factors to characterize the lung fibrogenic microenvironment for autonomous tissue reconstruction. The essential factors might be different among cell types. For AT2 cells, a previous study identified a unique mesenchymal cell population termed mesenchymal alveolar niche cells (MANCs) (Zepp et al., 2017). These cells reside close to AT2 cells *in vivo* and promote AT2 cell proliferation and differentiation *in vitro*. MANCs were apparently located around areas of αSMA$^+$ myofibroblast accumulation in BLM-injured lungs (Zepp et al., 2017), suggesting the possible contribution of MANCs to alveolar reconstitution by AT2 cells. Second, it is unknown whether the general population or only a certain specific subpopulation of AT2 cells contributes to the resolution of fibrosis. Our AT2 cell isolation strategy for transplantation is characterized by depletion of bronchial cells to purify mature AT2 cells; therefore, the possibility of club cell contamination, which then differentiate into AT2 cells, would be eliminated (Hasegawa et al., 2017). Alveolar epithelial progenitors (AEPs) identified by Zacharias et al. and characterized by the cell surface marker Tm4sf1 (Zacharias et al., 2018) are possible candidates. Recently, Choi et al. identified *Il1ra*$^+$ AT2 cells that were specifically primed in response to inflammatory signals after lung injury to regenerate alveolar epithelial cells (Choi et al., 2020), which may also play a role in our model. Sorting these subpopulations of AT2 cells may enhance

engraftment efficiency and potentially maximize the regenerative effect, which needs further study. Third, the applicability of the L-PDX model was not thoroughly evaluated in this study. Although histological similarities suggest the maintenance of the original tumor properties in our L-PDX model, a comprehensive evaluation, such as transcriptome analysis or response to pharmacological intervention, would be needed. In addition, the establishment of an L-PDX model from more small specimens, such as biopsy specimens, would be clinically anticipated.

STAR★METHODS

Detailed methods are provided in the online version of this paper and include the following:

- KEY RESOURCES TABLE
- RESOURCE AVAILABILITY
  - ○ Lead contact
  - ○ Materials availability
  - ○ Data and code availability
- EXPERIMENTAL MODEL AND SUBJECT DETAILS
- METHOD DETAILS
  - ○ Cell lines and reagents
  - ○ Animals
  - ○ Bleomycin (BLM)-induced lung injury
  - ○ The preparation of single-cell suspensions of murine lung
  - ○ The preparation of single-cell suspensions of human lung parenchyma or cancer tissue
  - ○ Flow cytometric analysis and sorting of lung cells
  - ○ Immunohistological analysis
  - ○ Immunofluorescence analysis
  - ○ Hydroxyproline assay
  - ○ AT2 fibroblast coculture
  - ○ AT2 cell transplantation
  - ○ RNA purification
  - ○ Microarray analysis
  - ○ Real-time (RT) PCR
  - ○ Gene ontology analysis
  - ○ Micro-CT imaging
- QUANTIFICATION AND STATISTICAL ANALYSIS
  - ○ Statistical analysis

SUPPLEMENTAL INFORMATION

Supplemental information can be found online at https://doi.org/10.1016/j.isci.2022.104912.

AUTHOR CONTRIBUTIONS

RM: Conceptualization, methodology, investigation, formal analysis, writing – original draft, and visualization. KH: Conceptualization, methodology, investigation, formal analysis, writing – original draft, and visualization. TM: Writing – review and editing. AY: Formal analysis, visualization, writing – review and editing. AW: Writing – review and editing. TH: Writing – review and editing. HD: Writing – review and editing. AS: Conceptualization, methodology, supervision, funding acquisition, and writing – review and editing.

DECLARATION OF INTERESTS

The authors have no financial conflicts of interest.

iScience
Article

REFERENCES

Bankert, R.B., Hess, S.D., and Egilmez, N.K. (2002). SCID mouse models to study human cancer pathogenesis and approaches to therapy: potential, limitations, and future directions. Front. Biosci. 7. c44–62.

Barkauskas, C.E., Cronce, M.J., Rackley, C.R., Bowie, E.J., Keene, D.R., Stripp, B.R., Randell, S.H., Noble, P.W., and Hogan, B.L. (2013). Type 2 alveolar cells are stem cells in adult lung. J. Clinical Investig. 123, 3025–3036. https://doi.org/10.1172/jci68782.

Berman, J.S., Serlin, D., Li, X., Whitley, G., Hayes, J., Rishikof, D.C., Ricupero, D.A., Liaw, L., Goetschkes, M., and O'Regan, A.W. (2004). Altered bleomycin-induced lung fibrosis in osteopontin-deficient mice. Am. J. Physiol. Lung Cell Mol. Physiol. 286, L1311–L1318. https://doi.org/10.1152/ajplung.00394.

Bibby, M.C. (2004). Orthotopic models of cancer for preclinical drug evaluation: advantages and disadvantages. Eur. J. Cancer 40, 852–857. https://doi.org/10.1016/j.ejca.2003.11.021.

Borok, Z., Gillissen, A., Buhl, R., Hoyt, R.F., Hubbard, R.C., Ozaki, T., Rennard, S.I., and Crystal, R.G. (1991). Augmentation of functional prostaglandin E levels on the respiratory epithelial surface by aerosol administration of prostaglandin E. Am. Rev. Resp. Dis. 144, 1080–1084. https://doi.org/10.1164/ajrccm/144.5.1080.

Carey, W.A., Taylor, G.D., Dean, W.B., and Bristow, J.D. (2010). Tenascin-C deficiency attenuates TGF-ss-mediated fibrosis following murine lung injury. Am. J. Physiol. 299, L785–L793. https://doi.org/10.1152/ajplung.00385.

Chen, L., Acciani, T., Le Cras, T., Lutzko, C., and Perl, A.K. (2012). Dynamic regulation of platelet-derived growth factor receptor alpha expression in alveolar fibroblasts during realveolarization. Am. J. Resp. Cell Mol. Biol. 47, 517–527. https://doi.org/10.1165/rcmb.2012-0030OC.

Chijiwa, T., Kawai, K., Noguchi, A., Sato, H., Hayashi, A., Cho, H., Shiozawa, M., Kishida, T., Morinaga, S., Yokose, T., et al. (2015). Establishment of patient-derived cancer xenografts in immunodeficient NOG mice. Int. J. Oncol. 47, 61–70. https://doi.org/10.3892/ijo.2015.2997.

Choi, J., Park, J.E., Tsagkogeorga, G., Yanagita, M., Koo, B.K., Han, N., and Lee, J.H. (2020). Inflammatory signals induce AT2 cell-derived damage-associated transient progenitors that mediate alveolar regeneration. Cell Stem Cell 27, 366–382.e7. https://doi.org/10.1016/j.stem.2020.06.020.

Cross, D.A., Ashton, S.E., Ghiorghiu, S., Eberlein, C., Nebhan, C.A., Spitzler, P.J., Orme, J.P., Finlay, M.R., Ward, R.A., Mellor, M.J., et al. (2014). AZD9291, an irreversible EGFR TKI, overcomes T790M-mediated resistance to EGFR inhibitors in lung cancer. Cancer Discov. 4, 1046–1061. https://doi.org/10.1158/2159-8290.CD-14-0337.

Fehrenbach, H. (2001). Alveolar epithelial type II cell: defender of the alveolus revisited. Resp. Res. 2, 33–46.

Garcia-Prieto, E., Gonzalez-Lopez, A., Cabrera, S., Astudillo, A., Gutierrez-Fernandez, A., Fanjul-Fernandez, M., Batalla-Solis, E., Puente, X.S., Fueyo, A., Lopez-Otin, C., and Albaiceta, G.M. (2010). Resistance to bleomycin-induced lung fibrosis in MMP-8 deficient mice is mediated by interleukin-10. PLoS One 5, e13242. https://doi.org/10.1371/journal.pone.0013242.

Garcia, O., Hiatt, M.J., Lundin, A., Lee, J., Reddy, R., Navarro, S., Kikuchi, A., and Driscoll, B. (2016). Targeted type 2 alveolar cell depletion. A dynamic functional model for lung injury repair. Am. J. Resp. Cell Mol. Biol. 54, 319–330. https://doi.org/10.1165/rcmb.2014-0246OC.

Hagimoto, N., Kuwano, K., Nomoto, Y., Kunitake, R., and Hara, N. (1997). Apoptosis and expression of Fas/Fas ligand mRNA in bleomycin-induced pulmonary fibrosis in mice. Am. J. Resp. Cell Mol. Biol. 16, 91–101. https://doi.org/10.1165/ajrcmb.16.1.8998084.

Hasegawa, K., Sato, A., Tanimura, K., Uemasu, K., Hamakawa, Y., Fuseya, Y., Sato, S., Muro, S., and Hirai, T. (2017). Fraction of MHCII and EpCAM expression characterizes distal lung epithelial cells for alveolar type 2 cell isolation. Resp. Res. 18, 150. https://doi.org/10.1186/s12931-017-0635-5.

Hay, J., Shahzeidi, S., and Laurent, G. (1991). Mechanisms of bleomycin-induced lung damage. Arch. Toxicol. 65, 81–94.

Helene, M., Lake-Bullock, V., Zhu, J., Hao, H., Cohen, D.A., and Kaplan, A.M. (1999). T cell independence of bleomycin-induced pulmonary fibrosis. J. Leukoc. Biol. 65, 187–195.

Herzog, E.L., Brody, A.R., Colby, T.V., Mason, R., and Williams, M.C. (2008). Knowns and unknowns of the alveolus. Proc. Am. Thorac. Soc. 5, 778–782. https://doi.org/10.1513/pats.200803-028HR.

Karampitsakos, T., Tzilas, V., Tringidou, R., Steiropoulos, P., Aidinis, V., Papiris, S.A., Bouros, D., and Tzouvelekis, A. (2017). Lung cancer in patients with idiopathic pulmonary fibrosis. Pulm. Pharmacol. Therapeut. 45, 1–10. https://doi.org/10.1016/j.pupt.2017.03.016.

King, B.A., and Kingma, P.S. (2011). Surfactant protein D deficiency increases lung injury during endotoxemia. Am. J. Resp. Cell Mol. Biol. 44, 709–715. https://doi.org/10.1165/rcmb.2009-0436OC.

Lama, V., Moore, B.B., Christensen, P., Toews, G.B., and Peters-Golden, M. (2002). Prostaglandin E2 synthesis and suppression of fibroblast proliferation by alveolar epithelial cells is cyclooxygenase-2-dependent. Am. J. Resp. Cell Mol. Biol. 27, 752–758. https://doi.org/10.1165/rcmb.4857.

Mediavilla-Varela, M., Boateng, K., Noyes, D., and Antonia, S.J. (2016). The anti-fibrotic agent pirfenidone synergizes with cisplatin in killing tumor cells and cancer-associated fibroblasts. BMC Cancer 16, 176. https://doi.org/10.1186/s12885-016-2162-z.

Moeller, A., Ask, K., Warburton, D., Gauldie, J., and Kolb, M. (2008). The bleomycin animal model: a useful tool to investigate treatment options for idiopathic pulmonary fibrosis? Int. J. Biochem. Cell Biol. 40, 362–382. https://doi.org/10.1016/j.biocel.2007.08.011.

Mulugeta, S., Nureki, S.I., and Beers, M.F. (2015). Lost after translation: insights from surfactant for understanding the role of alveolar epithelial dysfunction and cell quality control in fibrotic lung disease. Am. J. Physiol. Lung Cell. Mol. Physiol. https://doi.org/10.1152/ajplung.00139.2015.

Nureki, S.I., Tomer, Y., Venosa, A., Katzen, J., Russo, S.J., Jamil, S., Barrett, M., Nguyen, V., Kopp, M., Mulugeta, S., and Beers, M.F. (2018). Expression of mutant Sftpc in murine alveolar epithelia drives spontaneous lung fibrosis. The Journal of Clin. Investig. 128, 4008–4024. https://doi.org/10.1172/jci99287.

Panos, R.J., Bak, P.M., Simonet, W.S., Rubin, J.S., and Smith, L.J. (1995). Intratracheal instillation of keratinocyte growth factor decreases hyperoxia-induced mortality in rats. J. Clin. Investig. 96, 2026–2033. https://doi.org/10.1172/jci118250.

Povedano, J.M., Martinez, P., Flores, J.M., Mulero, F., and Blasco, M.A. (2015). Mice with pulmonary fibrosis driven by telomere dysfunction. Cell Rep. 12, 286–299. https://doi.org/10.1016/j.celrep.2015.06.028.

Rock, J.R., Barkauskas, C.E., Cronce, M.J., Xue, Y., Harris, J.R., Liang, J., Noble, P.W., and Hogan, B.L. (2011). Multiple stromal populations contribute to pulmonary fibrosis without evidence for epithelial to mesenchymal transition. Prod. Natl. Acad. of Sci. USA 108, E1475–E1483. https://doi.org/10.1073/pnas.1117988108.

Rogliani, P., Calzetta, L., Cavalli, F., Matera, M.G., and Cazzola, M. (2016). Pirfenidone, nintedanib and N-acetylcysteine for the treatment of idiopathic pulmonary fibrosis: a systematic review and meta-analysis. Pulm. Pharmacol. Therapeut. 40, 95–103. https://doi.org/10.1016/j.pupt.2016.07.009.

Sahai, E., Astsaturov, I., Cukierman, E., DeNardo, D.G., Egeblad, M., Evans, R.M., Fearon, D., Greten, F.R., Hingorani, S.R., Hunter, T., et al. (2020). A framework for advancing our understanding of cancer-associated fibroblasts. Nat. Rev. Cancer 20, 174–186. https://doi.org/10.1038/s41568-019-0238-1.

Sgalla, G., Iovene, B., Calvello, M., Ori, M., Varone, F., and Richeldi, L. (2018). Idiopathic pulmonary fibrosis: pathogenesis and management. Resp. Res. *19*, 32. https://doi.org/10.1186/s12931-018-0730-2.

Sisson, T.H., Mendez, M., Choi, K., Subbotina, N., Courey, A., Cunningham, A., Dave, A., Engelhardt, J.F., Liu, X., White, E.S., et al. (2010). Targeted injury of type II alveolar epithelial cells induces pulmonary fibrosis. Am. J. Respir. Crit. Care Med. *181*, 254–263. https://doi.org/10.1164/rccm.200810-1615OC.

Suzuki, H., Nagai, K., Yamaki, H., Tanaka, N., and Umezawa, H. (1969). On the mechanism of action of bleomycin: scission of DNA strands in vitro and in vivo. J. Antibiotics *22*, 446–448.

Taguchi, F., Koh, Y., Koizumi, F., Tamura, T., Saijo, N., and Nishio, K. (2004). Anticancer effects of ZD6474, a VEGF receptor tyrosine kinase inhibitor, in gefitinib ("Iressa")-sensitive and resistant xenograft models. Cancer Sci. *95*, 984–989.

Tang, N., Zhao, Y., Feng, R., Liu, Y., Wang, S., Wei, W., Ding, Q., An, M.S., Wen, J., and Li, L. (2014). Lysophosphatidic acid accelerates lung fibrosis by inducing differentiation of mesenchymal stem cells into myofibroblasts. J. Cell Mol. Med. *18*, 156–169. https://doi.org/10.1111/jcmm.12178.

Tsukui, T., Ueha, S., Abe, J., Hashimoto, S., Shichino, S., Shimaoka, T., Shand, F.H., Arakawa, Y., Oshima, K., Hattori, M., et al. (2013). Qualitative rather than quantitative changes are hallmarks of fibroblasts in bleomycin-induced pulmonary fibrosis. Am. J. Pathol. *183*, 758–773. https://doi.org/10.1016/j.ajpath.2013.06.005.

Tsukui, T., Ueha, S., Shichino, S., Inagaki, Y., and Matsushima, K. (2015). Intratracheal cell transfer demonstrates the profibrotic potential of resident fibroblasts in pulmonary fibrosis. Am. J. Pathol. *185*, 2939–2948. https://doi.org/10.1016/j.ajpath.2015.07.022.

Wang, R., Ibarra-Sunga, O., Verlinski, L., Pick, R., and Uhal, B.D. (2000). Abrogation of bleomycin-induced epithelial apoptosis and lung fibrosis by captopril or by a caspase inhibitor. Am. J. Physiol. *279*, L143–L151.

Weng, T., Poth, J.M., Karmouty-Quintana, H., Garcia-Morales, L.J., Melicoff, E., Luo, F., Chen, N.Y., Evans, C.M., Bunge, R.R., Bruckner, B.A., et al. (2014). Hypoxia-induced deoxycytidine kinase contributes to epithelial proliferation in pulmonary fibrosis. Am. J. Respir. Crit. Care Med. *190*, 1402–1412. https://doi.org/10.1164/rccm.201404-0744OC.

Yi, E.S., Williams, S.T., Lee, H., Malicki, D.M., Chin, E.M., Yin, S., Tarpley, J., and Ulich, T.R. (1996). Keratinocyte growth factor ameliorates radiation- and bleomycin-induced lung injury and mortality. Am. J. Pathol. *149*, 1963–1970.

Zacharias, W.J., Frank, D.B., Zepp, J.A., Morley, M.P., Alkhaleel, F.A., Kong, J., Zhou, S., Cantu, E., and Morrisey, E.E. (2018). Regeneration of the lung alveolus by an evolutionarily conserved epithelial progenitor. Nature *555*, 251–255. https://doi.org/10.1038/nature25786.

Zepp, J.A., Zacharias, W.J., Frank, D.B., Cavanaugh, C.A., Zhou, S., Morley, M.P., and Morrisey, E.E. (2017). Distinct mesenchymal lineages and niches promote epithelial self-renewal and myofibrogenesis in the lung. Cell *170*, 1134–1148.e10. https://doi.org/10.1016/j.cell.2017.07.034.

Zheng, D., Limmon, G.V., Yin, L., Leung, N.H., Yu, H., Chow, V.T., and Chen, J. (2012). Regeneration of alveolar type I and II cells from Scgb1a1-expressing cells following severe pulmonary damage induced by bleomycin and influenza. PLoS One *7*, e48451. https://doi.org/10.1371/journal.pone.0048451.

STAR★METHODS

KEY RESOURCES TABLE

REAGENT or RESOURCE	SOURCE	IDENTIFIER
Antibodies		
Rat CD45-PE-Cy7 (Clone: 30-F11)	eBioscience	Cat# 25-0451-82
Rat CD31-PE-Cy7 (Clone: 390)	BD Biosciences	Cat# 561410
Rat EpCAM-APC (Clone: G8.8)	eBioscience	Cat# 17-5791-82
Rat EpCAM-FITC (Clone: G8.8)	eBioscience	Cat# 11-5791-82
Rat MHCII-eFluor450 (Clone: I-A/I-E)	eBioscience	Cat# 48-5321-82
Mouse HLA-DR-eFluor450 (Clone: LN3)	Thermo Fisher	Cat# 48-9956-42
Mouse EpCAM-eFluor660 (Clone: 1B7)	Thermo Fisher	Cat# 50-9326-42
Mouse CD45-PE-Cy7 (Clone: 2D1)	Thermo Fisher	Cat# 25-9459-41
Mouse CD31-PE-Cy7 (Clone: WM059)	Thermo Fisher	Cat# 25-0319-41
Mouse Rabbit proSP-C	Millipore	Cat# AB3796
Rat Ki-67-FITC (Clone: SolA15)	eBioscience	Cat# 11-5698-80
Mouse anti-proSP-C	Abcam	Cat# ab40879
Mouse anti-STEM121	TaKaRa	Cat# Y40410
Mouse anti-Human Nucleoli	Abcam	Cat# ab190710
Rabbit anti-Ki-67	Millipore	Cat# AB9260
Hamster anti-podoplanin (T1α)	Abcam	Cat# ab11936
Rabbit anti-αSMA	Abcam	Cat# ab7817
Mouse anti-desmin	Abcam	Cat# ab6322
Rabbit anti-GFP	Abcam	Cat# ab183734
Rabbit anti-CD31	Abcam	Cat# ab28364
Bacterial and virus strains		
pEGFP-N1 vector	Dr Hisataka Sabe	RRID: Addgene_32751
Chemicals, peptides, and recombinant proteins		
Anti-mouse IgG1 Alexa Fluor 488	Thermo Fisher	Cat# A11001
Anti-rabbit IgG Alexa Fluor 594	Thermo Fisher	Cat# A11012
Anti-mouse IgG2a Alexa Fluor 647	Thermo Fisher	Cat# A28181
Lipofectamine 2000	Invitrogen	Cat# 11668019
Doxycycline-containing feed (600 ppm)	Oriental Yeast	Cat# D11072802
Tamoxifen	Toronto Research Chemicals	Cat# T006000
Bleomycin	Nihon Kayaku	CAS# 9041-93-4
Gefitinib	Selleck	Cat# S5098
Collagenasetype I	Gibco	Cat# 17100017
Dispase	Corning	Cat# 354235
DAPI	Life Technologies	Cat# 62248
Matrigel	Corning	Cat# 356234
Critical commercial assays		
GeneChip WT PLUS Reagent Kit	Affymetrix	Cat# 902280
GeneChip Mouse Gene 2.0 ST Array	Applied Biosystems	Cat# 902500
Clariom S Assay, Mouse	Applied Biosystems	Cat# 902931

Continued

REAGENT or RESOURCE	SOURCE	IDENTIFIER
Deposited data		
Microarray data (GeneChip Mouse Gene 2.0 ST Array)	This paper	GSE208444
Microarray data (Clariome S, Mouse)	This paper	GSE208373
Experimental models: Cell lines		
A549	ATCC	CCL-185
NCI-H441	ATCC	HTB-174
NCI-H1975	ATCC	CRL-5908
NCI-H226	ATCC	CRL-5826
NCI-H460	ATCC	HTB-177
NCI-H1299	ATCC	CRL-5803
PC-9	IBL cell bank	RRID: CVCL_B260
Lewis lung carcinoma	Taiho Pharmaceutical	RRID: CVCL_5653
Experimental models: Organisms/strains		
Mouse: C57/BL6J	The Jackson Laboratory	Strain code: 632
Mouse: CB17.Cg-Prkdc^{scid}Lyst^{bg-J}/CrlCrlj	The Jackson Laboratory	Strain code: 250
Mouse: C57BL/6-Tg (CAG-EGFP)	Dr Masataka Asagiri	Strain code: 329
Mouse: B6.Cg-Tg(Scgb1a1-rtTA)1Jaw/J	Dr Machiko Ikegami and Jeffrey A. Whitsett	Strain code: 6232
Mouse: B6;C3-Tg(ACTA1-rtTA, tetO-cre)102Monk/J	Dr Machiko Ikegami and Jeffrey A. Whitsett	Strain code: 12433
Mouse: ROSA$^{mT/mG}$	The Jackson Laboratory	Strain code: 37456
Mouse: Sftpc-CreER^{T2}	The Jackson Laboratory	Strain code: 28054
Mouse: Scgb1a1-CreER^{T2}	The Jackson Laboratory	http://www.informatics.jax.org/allele/MGI:5660121
Software and algorithms		
GeneSpring software version 13.1	Agilent Technologies	https://www.chem-agilent.com/contents.php?id=27881
Transcriptome Analysis Console Software version 4.0.1	Applied Biosystems	https://tools.thermofisher.com/content/sfs/brochures/tac_software_datasheet.pdf
Database for Annotation, Visualization, and Integrated Discovery (DAVID)	Laboratory of Human Retrovirology and Immunoinformatics	https://david.ncifcrf.gov/
SYNAPSE VINCENT software version 5	Fujifilm	https://www.fujifilm.com/jp/ja/healthcare/healthcare-it/it-3d/vincent
JMP ver. 10	SAS Institute	RRID:SCR_014242

RESOURCE AVAILABILITY

Lead contact

Further information and requests for resources and reagents should be directed to and will be fulfilled by the lead contact, Dr. Atsuyasu Sato (atsuyasu@kuhp.kyoto-u.ac.jp).

Materials availability

The study did not generate new unique reagents.

Data and code availability

- Microarray datasets have been deposited at GEO and are publicly available as of the date of publication. Accession numbers are listed in the key resources table.

- The paper does not report original code.

- Any additional information required to reanalyze the data reported in this paper is available from the lead contact on request.

EXPERIMENTAL MODEL AND SUBJECT DETAILS

The study protocols were approved by the Animal Research Committee of Kyoto University (ID: MedKyo 13533). Written informed consent for the use of lung parenchyma or cancer tissue and for subsequent use in the *in vivo* study was obtained according to a protocol approved by the Kyoto University Hospital Institutional Review Board (approved numbers: R1280 and R1486).

METHOD DETAILS

Cell lines and reagents

A549 (CCL-185), NCI-H441 (H441; HTB-174), NCI-H1975 (H1975; CRL-5908), NCI-H226 (H226; CRL-5826), NCI-H460 (H460; HTB-177), and NCI-H1299 (H1299; CRL-5803) cells were obtained from the American Type Culture Collection (Rockville, MD). PC-9 cells were obtained from the IBL cell bank (Gunma, Japan). Lewis lung carcinoma (LLC) cells were kindly supplied by Taiho Pharmaceutical (Tokyo, Japan). LLC-GFP was established by lipofection. The EGFP-N1 vector was kindly supplied by Dr Hisataka Sabe of Hokkaido University, Japan, and was transfected into LLC cells using Lipofectamine 2000 (Invitrogen, Cat. 11668019, Carlsbad, CA) according to the manufacturer's instructions. For the *in vivo* lung cancer treatment assay, mice were treated orally with a single bolus dose of either vehicle or gefitinib (Selleck Chemicals, Houston, TX).

Animals

Eight-week-old C57BL/6J mice (the Jackson Laboratory) and CB17.Cg-Prkdc^{scid}Lyst^{bg-J}/CrlCrlj mice (SCID-Beige mice) (the Jackson Laboratory) were purchased for use in this study. C57BL/6-Tg(CAG-EGFP) mice (GFP mice) were generously provided by Dr. Masataka Asagiri. Double-transgenic Scgb1a1-rtTA (Line 1)/(tetO)$_7$CMV-Cre mice (a gift from Dr Machiko Ikegami and Jeffrey A. Whitsett) were bred with ROSA$^{mT/mG}$ mice (the Jackson Laboratory) to generate triple-transgenic Scgb1a1-rtTA/(tetO)$_7$CMV-Cre/ROSA$^{mT/mG}$ mice. Doxycycline (600 ppm) was added to the chow starting from 5 weeks old to 8 weeks old to activate Cre-mediated recombination in triple-transgenic mice. Sftpc-CreER^{T2} mice (the Jackson Laboratory) or Scgb1a1-CreER^{T2} mice (the Jackson Laboratory) were bred with ROSA$^{mT/mG}$ mice to generate Sftpc-CreER^{T2}/ROSA$^{mT/mG}$ mice or Scgb1a1-CreER^{T2}/ROSA$^{mT/mG}$ mice. Tamoxifen (Toronto Research Chemicals, North York, Canada) was dissolved in corn oil (20 mg/ml) and injected intraperitoneally (200 mg/kg) for 4 consecutive days from 6 weeks old as previously reported (Barkauskas et al., 2013) to activate Cre-mediated recombination. The mice were used for experiments 2 weeks after tamoxifen injection.

Bleomycin (BLM)-induced lung injury

Mice were anaesthetized with isoflurane and hung upright at a 45-degree angle. BLM (Nihon Kayaku, Tokyo, Japan) (from 0.25 mg/kg to 2 mg/kg body weight in 100 μL of PBS) or PBS (control) was administered as reported previously (King and Kingma, 2011).

The preparation of single-cell suspensions of murine lung

For AT2 cell isolation, single lung cells were obtained as we previously reported (Hasegawa et al., 2017). For lung fibroblast isolation and analysis and cell sorting in the BLM model, protease solution [collagenase type I (450 U/ml; Gibco, Grand Island, NY) and dispase (5 U/ml; Corning, Corning, NY) in HBSS] was used, and whole lungs were incubated for 30 min at 37°C. The subsequent process was performed as we previously reported (Hasegawa et al., 2017).

The preparation of single-cell suspensions of human lung parenchyma or cancer tissue

Human lung parenchyma or cancer tissue was obtained from patients undergoing lung resection at Kyoto University Hospital because of lung cancer. All lung parenchyma or cancer samples were minced, transferred to the same protease mix as in the process of lung tissues in the murine BLM model, and incubated at 37°C for 60 min. The subsequent steps were the same as in the preparation of a single-cell suspension of murine lung (Hasegawa et al., 2017). Pathological evaluation for the establishment of xenografts was reviewed for consistency by a single pathologist (A.Y.).

Flow cytometric analysis and sorting of lung cells

Antibodies used for flow cytometry are listed in Key resources table. We sorted live, single cells using a FACSAria III Cell Sorter with FACSDiva ver. 8.0.1 (BD Biosciences). Murine AT2 cells were identified and sorted as we previously reported, with a purity >98% (Hasegawa et al., 2017). Human AT2 cells were identified as $CD45^-CD31^-EpCAM^+HLA\text{-}DR^+$ cells using the same gating strategy as murine AT2 cells (Hasegawa et al., 2017). Murine lung mesenchymal cells were identified as $CD45^-CD31^-EpCAM^-$ cells as described previously (Zepp et al., 2017). Sorted cells were collected in DMEM containing 10% FBS, antibiotics, antimycotic solution, and 25 mM HEPES (Life Technologies, Gaithersburg, MD) for further experiments. For intracellular staining, the cells were incubated with the fixable viability dye eFluor780 (eBioscience) and surface antigens, fixed, and permeabilized with fixation and permeabilization buffer (eBioscience) according to the manufacturer's instructions. Permeabilized cells were incubated with anti-Ki-67 antibody and anti-proSP-C antibody. Anti-mouse proSP-C antibody was labelled with PE-antirabbit IgG antibody. Fixed cells were analyzed using a BD LSR Fortessa (BD Biosciences). Appropriate isotype control samples were utilized for all FACS analyses. The data were analyzed using FlowJo software (ver. 7.6.5, Tree Star, San Carlos, CA).

Immunohistological analysis

The antibodies used for immunohistochemistry are listed in Key resources table. Murine lungs were inflated, fixed at 25 cm H_2O with 10% neutral buffered formalin and embedded in paraffin. Tissue sections (4-μm thick) were immunostained with primary antibodies at 4°C overnight followed by incubation with horseradish peroxidase (HRP)-conjugated secondary antibodies. Immunoreactivity was visualized by incubation with 3,3'-diaminobenzidine (DAB).

Immunofluorescence analysis

Antibodies used for immunofluorescence are listed in Key resources table. Murine lungs were inflated, fixed at 25 cm H_2O with 10% neutral buffered formalin and embedded in paraffin. Tissue sections (4-μm thick) were immunostained with primary antibodies. Alexa 488-, Alexa 594-, and Alexa 647-conjugated secondary antibodies (1:200; Life Technologies) were used for immunofluorescence analysis. Tissue slides were mounted with anti-fade solution containing DAPI (Life Technologies). Fluorescence images were obtained using an LSM 710 confocal microscope (Carl Zeiss, Thornwood, NY), an SP-8 confocal microscope (Leica Microsystems, Wetzlar, Germany), or a BIOREVO BZ-9000/BZ-X810 fluorescence microscope (Keyence, Osaka, Japan).

Hydroxyproline assay

Mice were sacrificed, and the right lungs or whole lungs were harvested for the assay. The lungs were transferred to gentleMACS M tubes (Miltenyi Biotech) containing 1.5 mL (for right lungs) or 3 ml (for whole lungs) of saline and homogenized using the gentleMACS Dissociator program RNA-01. Then, 300 μl of lung homogenate was mixed with 300 μL of 12 N HCl and heated overnight at 107°C. Next, 20 μL of acid hydrolysates was mixed with 20 μL of citrate-acetate buffer and 400 μL of chloramine T solution and incubated for 20 min at room temperature. Then, 400 μL of aldehyde/perchloric acid solution was added to the tubes, vortexed and incubated for 15 min at 65°C before measurement of the absorbance (optical density OD_{560}).

AT2 fibroblast coculture

AT2 fibroblast coculture was performed according to a previous study (Barkauskas et al., 2013) with a slight modification. Briefly, sorted AT2 cells (5×10^3) and lung mesenchymal cells (1×10^5) were resuspended in 50 μL of the medium and mixed with 50 μL of growth factor-reduced Matrigel (Corning). Then, 100 μL of mixed cell suspension was placed in a 24-well 0.4-μm Transwell insert (Falcon), and 500 μL of the medium was placed in the lower chamber. Cells were incubated at 37°C in a 5% CO_2 environment, and the medium was changed every other day. Y-27632 (10 μM) was added to the medium for the first 2 days of culture. Immunofluorescence of AT2 colonies was performed as whole mount staining. Matrigel disks were fixed with 4% paraformaldehyde in PBS for 15min at RT and then washed with PBS prior to blocking and immunostaining, as was done for the immunofluorescence staining of tissue sections.

AT2 cell transplantation

On day 10 after BLM treatment, mice were administered 4.0×10^5 freshly isolated AT2 cells suspended in 100 μL of PBS following the same procedure as for BLM administration. The control group received 100 μL of PBS.

RNA purification

Total RNA was purified using an RNeasy mini plus kit (Qiagen, Chatsworth, CA) according to the manufacturer's protocol. The integrity of total RNA was assessed using an Agilent 2100 Bioanalyzer (Agilent Technologies, Palo Alto, CA), and samples with an RNA integrity number (RIN) above 8.0 were used for further analyses.

Microarray analysis

Total RNA samples (100 ng) were processed with a GeneChip WT PLUS Reagent Kit (Affymetrix) and hybridized to a GeneChip Mouse Gene 2.0 ST Array for mesenchymal cell analysis or to a Clariom S Assay for cancer cell analysis according to the manufacturer's protocol. Raw data obtained with Affymetrix GeneChip Operating Software were normalized and analyzed by GeneSpring software (version 13.1, Agilent Technologies, Santa Clara, CA, USA) for mesenchymal cell analysis or Transcriptome Analysis Console Software (version 4.0.1, Applied Biosystems, CA, USA) for cancer cell analysis.

Real-time (RT) PCR

cDNA was synthesized from purified total RNA using an iScript cDNA synthesis kit (Bio-Rad Laboratories, Hercules, CA). Quantitative RT-PCR was performed using TaqMan Gene Expression Assays and a StepOne Plus Real-Time PCR ystem (Life Technologies).

Gene ontology analysis

The differentially expressed genes were subjected to gene ontology (GO) analysis using the Database for Annotation, Visualization, and Integrated Discovery (DAVID) to find overrepresentations of GO terms in the biological process (BP) category (GOTERM_BP_FAT, GOTERM_CC_FAT, and GOTERM_MF_FAT) (https://david.ncifcrf.gov/. Accessed on November 27th, 2018). As background, the *Mus musculus* (mouse) whole genome was used (Mm9). Statistical enrichment was determined using the default settings in DAVID.

Micro-CT imaging

Mice were anaesthetized with a continuous flow of 4% isoflurane/air mixture (2.0 L/min) and placed in the chamber of the micro-CT system (LaTheta LCT-200, Aloka, Tokyo, Japan). The processing of the CT data was performed using ImageJ software (ver.1.52a, National Institutes of Health, Bethesda, MD, USA). The tumor volume was semi-automatically obtained using SYNAPSE VINCENT software (Fujifilm Co. Tokyo, Japan).

QUANTIFICATION AND STATISTICAL ANALYSIS

Statistical analysis

The values are expressed as the means $\pm$ SEM if not otherwise specified. Statistical analyses were performed using JMP (ver.10, SAS Institute, Cary, NC). Comparisons between two groups were performed using the Wilcoxon rank sum test. The differences between more than two groups were analyzed with analysis of variance, and post hoc analysis was performed using the Tukey–Kramer test. GeneSpring software (ver.13.1, Agilent Technologies, Santa Clara, USA) and Transcriptome Analysis Console Software (ver.4.0.1, Applied Biosystems, California, USA) were used for microarray analysis. The processing of the CT data was performed using ImageJ software (ver.1.52a, National Institutes of Health, Bethesda, MD, USA). SYNAPSE VINCENT software (ver.5, Fujifilm Co. Tokyo, Japan) was used for the 3-D reconstruction of CT images and calculation of tumor volume. The exact number of replicates in each group and the statistical tests used were specified in Figure legends.